

1 **Chromatin-lamin B1 interaction promotes genomic**
2 **compartmentalization and constrains chromatin dynamics**

3 Lei Chang^{1§}, Mengfan Li^{2,3§}, Shipeng Shao^{1§}, Boxin Xue¹, Yingping Hou^{2,3}, Yiwen Zhang¹,
4 Ruifeng Li^{2,3}, Cheng Li^{3,4*}, Yujie Sun^{1*}

5 ¹ State Key Laboratory of Membrane Biology, School of Life Sciences, and Biomedical
6 Pioneering Innovation Center (BIOPIC), Peking University, Beijing, China, 100871

7 ² Peking-Tsinghua Center for Life Sciences, Academy for Advanced Interdisciplinary
8 Studies, Peking University, Beijing, 100871

9 ³ Center for Bioinformatics, School of Life Sciences, Peking University, Beijing, 100871

10 ⁴ Center for Statistical Science, Peking University, Beijing, 100871

11 [§] These authors contributed equally to this work.

12 * Corresponding author. Email: sun_yujie@pku.edu.cn (Y.S.); cheng_li@pku.edu.cn (C.L.)

13 **Abstract**

14 The eukaryotic genome is folded into higher-order conformation accompanied with
15 constrained dynamics for coordinated genome functions. However, the molecular
16 machinery underlying these hierarchically organized chromatin architecture and dynamics
17 remains poorly understood. Here by combining imaging and Hi-C sequencing, we studied
18 the role of lamin B1 in chromatin architecture and dynamics. We found that lamin B1
19 depletion leads to chromatin redistribution and decompaction. Consequently, the inter-
20 chromosomal interactions and overlap between chromosome territories are increased.

21 Moreover, Hi-C data revealed that lamin B1 is required for the integrity and segregation of
22 chromatin compartments but not for the topologically associating domains (TADs). We
23 further proved that depletion of lamin B1 leads to increased chromatin dynamics, owing to
24 chromatin decompaction and redistribution toward nuclear interior. Taken together, our
25 data suggest that chromatin-lamin B1 interactions promote chromosomal territory
26 segregation and genomic compartmentalization, and confine chromatin dynamics,
27 supporting its crucial role in chromatin higher-order structure and dynamics.

28 **Introduction**

29 Chromatin in the interphase nucleus of eukaryotic cells are highly compartmentalized and
30 structured. Owing to technological breakthroughs in imaging(1-3) and sequencing(4-9),
31 chromatin higher-order structure has been increasingly studied over the last decade.
32 Hierarchical chromatin architecture is composed of loops, TADs, active and inactive A/B
33 compartments, and chromosome territories, in increasing scales. A number of architectural
34 proteins and molecular machineries governing chromatin organization and dynamics have
35 been identified. For instance, CTCF(10) and cohesin(11-14) are partly responsible for the
36 formation and maintenance of chromatin loops and TADs. Nevertheless, CTCF does not
37 impact higher-order genomic compartmentalization and cohesin even limits segregation of
38 A/B compartments(15). Until now, the mechanisms that underlie the insulation and
39 distribution of A/B compartments and chromosome territories remain elusive.

40 Microscopy and chromosome conformation capture techniques provide
41 complementary insights into chromatin higher-order structure and sub-nuclear chromatin
42 spatial distribution. Genomic regions that belong to A-compartments identified by Hi-C
43 are gene rich, enriched with euchromatin histone markers and transcriptionally active(7,

44 16). Microscopy reveals that transcriptionally active euchromatic loci prefer to localize in
45 nuclear interior(17). On the contrary, B-compartments identified by Hi-C are gene poor,
46 enriched with heterochromatin markers, and frequently associated with the nuclear
47 lamina(7, 16). These findings are concordant with imaging results that transcriptionally
48 inactive heterochromatin is mainly found near nuclear periphery and nucleoli(17). In
49 addition, chromosome territories also show nuclear location preference, in which gene-rich
50 chromosomes are generally situated towards the interior and gene-poor chromosomes
51 towards the periphery of the nucleus(18). Such spatial correlations make nuclear lamina a
52 plausible candidate that contributes to the segregation and sub-nuclear distribution of A/B
53 compartments and chromosome territories(19-21). Despite these insights, whether lamina
54 proteins are responsible for the segregation and localization of higher-order chromatin
55 structure remains unknown.

56 Besides the hierarchical structure, motion is another basic physical property of
57 chromatin. Live cell fluorescence imaging in the nucleus can provide abundant information
58 on the dynamics of whole chromosomes, chromosomal loci, transcription factors etc.(22).
59 For instance, analyzing the motion of chromosomal loci embedded within viscoelastic
60 nucleoplasm is a valuable technique for extracting micro-environmental properties and
61 obtaining information of genomic organization and functions. Actually, the diffusion
62 dynamics of genomic loci are not mere Brownian motion driven by thermal fluctuation but
63 are often convoluted with active processes such as transcription and DNA repair(23-27).
64 So far, most studies on genomic loci dynamics have been carried out in bacteria(28, 29)
65 and yeast(30-33). In yeast, chromatin dynamics appear to be determined by nuclear
66 constraints. In particular, the telomeres and centromeres are known to be tethered to nuclear

67 envelope, which is suggested to contribute to chromosome territory segregation(34). For
68 mammalian cells, previous studies have shown that chromatin motion is a constrained
69 diffusion process that is associated with nuclear localization(35), and loss of lamin A
70 increases chromatin dynamics in the nuclear interior as well as nuclear periphery(36).
71 However, it is unclear how this sub-diffusion is related to chromatin higher-order structure,
72 and it is not known whether tethering between the nuclear envelop and chromatin functions
73 similarly as in yeast.

74 Nuclear lamina consists of many protein complexes, and lamins are the main
75 components of nuclear lamina in most mammalian cells and can be classified into A- and
76 B-type lamins. Lamin A and C are the most common A-type lamins and are splice variants
77 of the same gene, while B-type lamins, B1 and B2, are the products of two different
78 genes(37). Lamin B1 mainly localizes at the nuclear periphery, while A-type lamins are
79 also found in the nucleoplasm(38). DamID of lamin B1 has revealed many nuclear lamina-
80 associated genomic regions named lamina-associated domains (LADs). Typically, a
81 mammalian genome contains 1100–1400 LADs and 71 % of the genome has conserved
82 relationship with lamina across different species, including 33% of constitutive LAD
83 (cLAD) and 38 % of constitutive inter-LAD (ciLAD)(39). Interestingly, lamin B1 has
84 structural domains that directly bind to DNA or histone and indirectly interact with
85 chromatin through LEM [LAP2 (lamina-associated polypeptide 2)/emerin/MAN1]
86 domain-containing proteins. Thus, lamin B1 can potentially provide anchors for chromatin
87 to regulate its position, higher-order structure and dynamics. Furthermore, lamina-
88 chromatin junction mediates the transduction of mechanical signals from cytoskeleton to

89 chromatin, possibly providing means for chromatin structures to respond to mechanical
90 forces(40, 41).

91 In this study, we hypothesized that chromatin-lamina interactions in mammalian
92 cells function in chromatin higher-order structure and dynamics. We applied a combination
93 of imaging and sequencing techniques to characterize the role of lamin B1 in chromatin
94 architecture and dynamics in human breast tumor cells. We found that lamin B1 is required
95 for segregation of chromosome territories and A/B compartments, but does not affect TAD
96 formation. Furthermore, depletion of lamin B1 or disruption of interaction between DNA
97 and lamin B1 can increase genomic loci dynamics, owing to chromosome decompaction
98 and redistribution toward nucleoplasm. Taken together, our data suggested that interactions
99 between lamin B1 and chromatin greatly contribute to chromatin compartmentalization,
100 compactness, spatial distribution and dynamics.

101 **Results**

102 **Lamin B1 depletion leads to chromatin redistribution and decompaction**

103 To explore the potential role of lamin B1 in nuclear chromatin organization, we first
104 investigated the subnuclear distribution of lamin B1 using super-resolution (STORM)
105 imaging. Lamin B1 was found to be almost exclusively located at the nuclear periphery
106 (fig. S1A), in contrast to A-type lamins which were located at both nuclear periphery and
107 nucleoplasm(36, 38). It was previously reported that lamin B1 interacts with chromatin
108 directly or via adaptor proteins(42). We then created a *LMNB1* (lamin B1 encoding gene)-
109 knockout MDA-MB-231 breast cancer cell line using the CRISPR-Cas9 genome editing
110 tool. Proper knockout of lamin B1 was confirmed by western blot and immunofluorescence

111 (fig. S1, A and B). Importantly, no apparent change of cell cycle was detected in lamin B1-
112 KO cells (fig. S1D), eliminating the possibility that alterations of nuclear organization are
113 due to biased cell cycle.

114 We reasoned that if the anchorage of chromatin to nuclear periphery is mediated by
115 the interaction with lamin B1, the loss of lamin B1 can lead to changes in distribution and
116 compaction of chromatin in the nucleus. To investigate the effect of lamin B1 on chromatin
117 spatial localization and compaction at the single chromosome level, we performed
118 chromosome painting for chromosomes 2 and 18 using FISH probes. Chromosomes 2 and
119 18 were chosen to represent chromosomes that are localized relatively near the nuclear
120 periphery and the nuclear interior, respectively. Previous studies described that gene-poor
121 chromosome 18 located toward the nuclear periphery and gene-dense chromosome 19 in
122 the nuclear interior(43, 44). However, Cremer et al. reported that in seven of eight cancer
123 cell lines, chromosome 18 located more internally than chromosome 19(45). Considering
124 the breast cancer cell line we used, we chose chromosome 18 to represent nuclear interior
125 localized chromosome rather than chromosome 19. In lamin B1-KO cells, chromosome 2
126 became significantly more centrally located while the position of chromosome 18 remained
127 at the nuclear interior (Fig. 1, A and B). In addition, compared with wild type cells, the
128 volume of both chromosomes were significantly increased in lamin B1-KO cells (Fig. 1,
129 A and C). This expansion of chromosome territories upon lamin B1 depletion is not due to
130 nuclear volume expansion (fig. S1E). These findings indicate that the nuclear location and
131 volume of individual chromosomes are affected in lamin B1-KO cells, and suggest that
132 loss of lamin B1 leads to redistribution and decompaction of the chromatin.

133 **Lamin B1 depletion reduces the segregation of chromosome territories and A/B**
134 **compartments**

135 Changes in location and volume of chromosomes may affect the territories between
136 chromosomes. Indeed, along with the redistribution and decompaction of chromatin, more
137 than 50% of lamin B1-KO cells showed overlap between the territories of chromosomes 2
138 and 18, compared with 15.1% in wild type cells (Fig. 1, A and D). This large-scale
139 reorganization of chromosome territories promoted us to investigate the role of lamin B1
140 in genome architecture using in situ Hi-C assay(46), which provides information about
141 multiscale chromatin interaction maps including chromosome compartments and TADs
142 (fig. S2, A and B, table S1). We first focused on inter-chromosomal interactions. In
143 agreement with the FISH results (Fig. 1, A and D), Hi-C data showed higher inter-
144 chromosomal interaction frequency between chromosomes 2 and 18 in lamin B1- KO cells
145 (Fig. 1E and fig. S2C), although the interaction frequency between different chromosomes
146 is much less than that within the same chromosome (table S1) as reported in previous
147 studies(7, 47). The inter-chromosomal interaction ratio of all chromosomes also showed a
148 significant increase in lamin B1-KO cells (Fig. 2, A and B). These results indicate that
149 lamin B1 contributes to the segregation of chromosome territories.

150 We next explored whether lamin B1-KO affects the organization of A and B
151 compartments, which are defined using the first principal component (PC1) of Hi-C
152 correlation matrices and correspond to different gene densities and transcriptional
153 activities(7) (Fig. 2C). Using super-resolution imaging, Zhuang and colleagues have shown
154 that adjacent A and B compartments are spatially separated from each other(2). Here,
155 although the Hi-C contact maps of the wild type and lamin B1-KO cells displayed similar

156 checkerboard patterns, the differential heatmap showed loss of intra-compartment
157 interactions (interactions between the A-A or B-B compartment pairs) and gain of inter-
158 compartment interactions (interactions between A-B compartment pairs) in lamin B1-KO
159 cells (Fig. 2C). We asked whether this change influences the interactions between specific
160 compartment types by computing the ratio of average interaction frequency between
161 different classes of compartments (AB) versus that between the same classes of
162 compartments (AA and BB) for each chromosome(48). These ratios showed significant
163 increase in lamin B1-KO cells (Fig. 2D), suggesting a crucial role of lamin B1 in
164 segregation of different compartment types. Moreover, 2.9% of genomic regions switched
165 from A compartment in wild type cells to B compartment in lamin B1-KO cells, while 3.9%
166 of genomic regions exhibited the opposite switching (Fig. 2, E and F). These percentages
167 of compartment switching upon lamin B1 depletion were higher than those between
168 replicates (fig. S2, D and E). These results indicate that lamin B1 contributes to the
169 formation and segregation of different chromosomal compartment types.

170 **Lamin B1 is not required for TAD insulation**

171 Within A/B compartments, chromatin is further packaged in the form of TADs, which are
172 considered as the basic structural units of chromatin and are largely conserved between cell
173 types and across species(49-51). We calculated insulation scores(51) for each 40 kb bin of
174 the Hi-C normalized matrix, and the local minima of insulation scores indicated TAD
175 boundaries. The contact maps and insulation scores of an example region on chromosome
176 10 showed similar TAD patterns in WT and lamin B1-KO cells (Fig. 3A). For the whole
177 genome, insulation scores were highly correlated between WT replicates (Pearson
178 correlation coefficient, $r=0.984$) or between lamin B1-KO replicates ($r=0.987$). Correlation

179 between WT and lamin B1-KO samples ($r=0.969$) was only slightly lower than that
180 between replicates (fig. S3A). Heatmaps showed that the distribution of insulation scores
181 around TAD boundaries was similar between WT and lamin B1-KO cells (Fig. 3, B and
182 C).

183 To investigate whether the TAD locations were changed upon lamin B1 depletion,
184 each TAD boundary in WT cells was paired with the most adjacent TAD boundary in lamin
185 B1-KO cells. We calculated the genomic distance between these paired TAD boundaries
186 and observed that 87% of the TAD boundaries located within the same or adjoining 40 kb
187 bins, and 92.3% of the TAD boundaries shifted by less than two 40 kb bins (Fig. 3D),
188 comparable to these percentages (95% and 95.8%) between WT or lamin B1-KO replicates.
189 The small number of TAD boundary pairs that are neither overlapping nor adjacent were
190 due to random variation upon the calculation of insulation scores (fig. S3, B and C). As a
191 result, WT and lamin B1-KO cells have almost overlapping TAD length distribution with
192 median length of 840 kb (Fig. 3E). Furthermore, we calculated the TAD score, which is
193 the ratio of intra-TAD interactions to overall cis-interactions, for each TAD, and found no
194 difference between WT and lamin B1-KO cells (fig. S3, D and E), indicating similar TAD
195 compactness for the two samples. Taken together, lamin B1 loss does not affect the
196 organization of TAD structures.

197 **Lamin B1 depletion changes the location preference of genomic loci**

198 To achieve high signal-to-noise ratio for precise localization and long-term imaging of
199 genomic loci, we developed CRISPR-SunTag, a site-specific chromatin labeling and
200 tracking system, in wild type and lamin B1-KO MDA-MB-231 cells (Fig. 4A and fig. S4,
201 A and B). To quantitatively categorize the position of genomic loci, we divided the nuclear

202 space into two regions of different transcription activities, i.e. nuclear periphery and
203 nucleoplasm (Fig. 4B and see Materials and Methods for details). Genomic loci imaging
204 showed that the same genomic loci could localize in different subnuclear regions (Fig. 4C)
205 but did demonstrate location preferences (Fig. 4D). For instance, the 1 Mb genomic locus
206 on chromosome 2 showed high percentage of nuclear peripheral localization (Fig. 4, C and
207 D), consistent with the overall peripheral location preference of chromosome 2 (Fig. 1, A
208 and B), while the 236 Mb locus on chromosome 2 showed low percentage of nuclear
209 peripheral localization (Fig. 4, C and D). In contrast, genomic loci on chromosome 18
210 tended to distribute in the nucleoplasm (Fig. 4, C and D). In order to avoid measurement
211 artifacts caused by projection from 3D to 2D, we compared the measured distances
212 between loci and nuclear envelope or nucleoli in 2D images and 3D image stacks and
213 obtained similar results (fig. S4, C and D). Thus, the overall location of genomic loci in the
214 nucleus coincides with their corresponding chromosome localization, but different loci on
215 the same chromosome have variable preferential subnuclear localization.

216 Lamin B1 depletion showed minimal effect on the preferential subnuclear
217 distribution of genomic loci on chromosome 18 but dramatically altered that on
218 chromosome 2, especially the loci near the nuclear periphery (Fig. 4, C and D). For
219 example, the percentage of the 1 Mb locus of chromosome 2 localized near the nuclear
220 periphery was greatly decreased in lamin B1 depleted cells (Fig. 4, C to E and fig. S4, E
221 and F). Lamin B1 may regulate the genomic loci distribution via direct/indirect binding
222 interaction or spatial confinement of accumulative nuclear lamina proteins in nuclear
223 periphery. To distinguish between these two possibilities, we constructed a plasmid
224 expressing a lamin B1 truncation protein missing the Ig-like domain. The Ig-like domain

225 is a conservative structure in lamin A/C and lamin B1(52), known as the motif that mediates
226 the direct/indirect interaction between lamins and DNA(42, 53) (fig. S4G). In contrast to
227 the exogenous full-length lamin B1 which could rescue the distribution preference of the 1
228 Mb locus on chromosome 2 in lamin B1-KO cells, the Ig-like domain-truncated lamin B1
229 failed to do so (Fig. 4E) even though it could still form the nuclear lamina (fig. S4H). These
230 results suggest that the tethering between lamin B1 and chromatin is important for the
231 subnuclear position of chromosomes and chromosomal loci.

232 **Loss of chromatin-lamin B1 interaction increases chromatin mobility**

233 Chromatin structures and transcriptional activities are intrinsically associated with its
234 dynamic motion(24, 27, 54). To further explore the influences of chromatin-lamin B1
235 interaction on the chromatin, we measured the chromatin dynamics in wild type and lamin
236 B1-KO cells. Three genomic loci consisting of telomeres, a locus localized at 1 Mb of
237 chromosome 2 and a locus at 14 Mb of chromosome 18, were labeled and successively
238 tracked in a short range of time scales (from 0.05 to 120 s) to minimize the artifacts caused
239 by cell deformation, migration or nucleus rotation (Movie). A customized tracking package
240 U-track(55) was used to extract the trajectories and mean square displacement (MSD) of
241 the loci. The data revealed that depletion of lamin B1 significantly increased the chromatin
242 dynamics compared with the slow anomalous diffusion in wild type cells of all three loci
243 (Fig. 5, A and B). Moreover, expressing exogenous lamin B1 in the knockout cell line
244 restored the loci dynamics to the level comparable to wild type cells (Fig. 5, C and D),
245 indicating that lamin B1 restricts chromatin dynamics. However, Ig-like domain-truncated
246 lamin B1 was not able to restore the loci dynamics in lamin B1-KO cells to the wild type

247 level as the full length lamin B1 did (Fig. 5, C and D), coinciding with the changes of loci
248 localization (Fig. 4E).

249 We next investigated how chromatin-lamin B1 interaction constrains chromatin
250 dynamics. We speculated that the redistribution of genomic loci in lamin B1-depleted cells
251 contributes to increased chromatin mobility. The above results promoted us to examine
252 whether the same locus in different subnuclear regions demonstrate different dynamic
253 mobility. Indeed, all three loci on chromosome 2 were much less mobile when located in
254 the nuclear periphery than in the nucleoplasm (Fig. 5, B and E), suggesting that the
255 dynamics of each locus is primarily influenced by their nuclear spatial environment.

256 Furthermore, we found that the motion of the 1 Mb locus on chromosome 2 in both
257 nuclear periphery and nucleoplasm became more active upon the depletion of lamin B1
258 (fig. S5A). Besides, the 14 Mb locus on chromosome 18, which only had nucleoplasm
259 distribution, also showed increased mobility in nucleoplasm in lamin B1-KO cells (Fig.
260 5A). These results indicate that lamin B1 restrains the mobility of genomic loci in both
261 nuclear periphery and nucleoplasm, not in line with the nuclear lamina distribution of lamin
262 B1. Thus, our data indicate that lamin B1 also constrains chromatin dynamics through other
263 ways, especially in the nucleoplasm.

264 **Chromatin decompaction mediates the effect of lamin B1 depletion on chromatin** 265 **dynamics**

266 Given the finding that lamin B1 depletion leads to chromatin decompaction (Fig. 1, A and
267 C), we next examined whether the increased chromatin dynamics upon loss of lamin B1
268 was due to chromatin decompaction. We treated wild type cells with Trichostatin A (TSA)

269 which can inhibit histone deacetylase enzyme and lead to genome-wide decondensation of
270 chromatin in both nuclear interior and periphery(56). To confirm the effect of chromatin
271 decompaction on chromosome spatial organization, we applied chromosome painting in
272 TSA-treated cells. We found that the relative volume of chromosomes increased
273 significantly compared with that in control cells (Fig. 6, A and B), but different from lamin
274 B1 depletion which also altered the position of chromosomes (Fig. 1, A and B), TSA
275 treatment did not change the radial distribution of chromosome territories (Fig. 6, A and
276 C). The overlap between chromosome 2 and 18 was also consequently increased in TSA-
277 treated cells compared with control cells (Fig. 6, A and D). We then measured the dynamic
278 mobility of chromosomal loci and found that TSA treatment indeed promoted the dynamic
279 mobility of chromosomal loci both near the nuclear periphery and within the nucleoplasm
280 (Fig. 6E and fig. S5B). Importantly, different from lamin B1 depletion, the sub-nuclear
281 distribution of the loci did not change in TSA-treated cells compared with DMSO-treated
282 control cells (Fig. 6F). These results suggest that chromatin compaction is key for
283 chromatin dynamics.

284 To further explore the relationship between chromatin dynamics and chromatin
285 compaction state, we chose 10 genomic loci on chromosome 2, 18 and 19 with 5 in A
286 compartments and 5 in B compartments (Fig. 6G). Tracking of the loci showed that the 5
287 loci belonging to A compartments (red) were more mobile than the 5 loci in B
288 compartments (blue) (Fig. 6, H and I), in line with the fact that A compartments are
289 generally less compact than B compartments. We also found that four genomic loci
290 belonging to A compartments in chromosome 18 and 19 had similar dynamic properties
291 and all of them localized in nucleoplasm (Fig. 6, H and I).

292 **Discussion**

293 Along with chromatin decompaction and relocation, the motion of genomic loci became
294 more active in lamin B1-depleted cells. In control cells, mobility of the same chromosomal
295 locus was found to be correlated with its subnuclear location in that genomic sites close to
296 lamina were generally less mobile than those localized in nuclear interior. These two lines
297 of evidence suggest that chromatin dynamics are dependent on both chromatin compaction
298 and loci location. However, when treating cells with TSA, which decompacts chromatin
299 but does not change its sub-nuclear distribution, we also found global increase of chromatin
300 mobility. Furthermore, in control cells, we consistently observed that chromosomal loci in
301 less compact compartment A were of higher mobility than that in more compact
302 compartment B, suggesting that chromatin compaction is more fundamental than
303 subnuclear location in regulating chromatin dynamics. This observation is consistent with
304 a recent theoretical work in which a model named MiChroM was proposed for the
305 formation of chromosomal spatial compartments(54). MiChroM defines dynamically
306 associated domains (DADs) in which the motions of genomic loci are correlated. DADs
307 are often found to be aligned with the A/B chromatin-type annotation and another study
308 proposed that the globally increased mobility of genomic loci may drive re-segregation at
309 the chromatin compartment level via modifying MiChroM(57). This theoretical work is
310 highly complementary with our experimental data, supporting the important role of
311 chromatin dynamics in higher-order chromatin organization.

312 The roles of lamins played on chromatin organization are less understood. Recently,
313 Leonid Mirny et al developed a polymer model of chromosomes to reconstruct chromatin
314 sub-nuclear localization in inverted and conventional nuclei(58). They found that

315 heterochromatin interactions with the lamina are essential for building conventional
316 nuclear architecture. In our study, we found that interaction between lamin B1 and
317 chromatin could drive the regulation of global chromatin structure (fig. S6). However,
318 regarding the nature of lamin B1-chromatin interaction, it is unclear whether the direct
319 binding or the confinement by the lamina meshwork mainly contributes to the regulation
320 of chromatin structure and dynamics. Here our work has provided several lines of evidence
321 to support the direct binding model. First, over-expressing Ig-like domain-truncated lamin
322 B1, which can still form meshwork, was not able to rescue the phenotype of chromatin
323 structure and dynamics caused by loss of lamin B1. Second, overexpressing lamin B1 did
324 not alter the chromatin dynamics. Therefore, it is intriguing to speculate that the tethering
325 and release of chromatin from lamina during each cell cycle might be an important process
326 to organize genome architecture.

327 Previous studies have shown that other protein components in lamina besides lamin
328 B1 also mediate its interactions with chromatin, including lamin A/C and LBR(59). Y.
329 Garini et al reported that depletion of lamin A can increase chromatin dynamics(36). They
330 emphasized that chromosomal inter-chain interactions formed by lamin A throughout the
331 nucleus is critical for the maintenance of genome organization but did not focus on the
332 tethering of chromatin with lamin A in the nuclear envelop. Interestingly, triple knockout
333 of lamins did not show effects on overall TAD structure but altered TAD-TAD interactions
334 in mESC(19), which is consistent with our results. However, lamins-KO mESCs had no
335 significant differences in the volumes and surface areas of chromosome 1 and 13, which is
336 different from previous studies and our results, indicating that lamins may play a stronger
337 role in maintaining chromatin structure in differentiated cells than in ESCs(19, 60). Thus,

338 the meshwork caging model they proposed may partially but not totally apply to
339 differentiated cell types. Further studies are needed to identify more functional proteins in
340 the lamina and their functional roles in chromatin structure and dynamics.

341 The nuclear matrix, which is hypothesized to provide a scaffold for chromatin
342 attachment and organize global chromatin structure in the nucleus, is composed of inner
343 and peripheral nuclear matrix. Recently, Hui Fan et al reported that the inner nuclear matrix
344 protein HNRNPU/SAF-A is involved in 3D genome organization(61). We compared our
345 lamin B1 data with their HNRNPU/SAF-A data and interestingly found that they contribute
346 to chromatin organization in an opposite manner, implicating some fundamental
347 coordinations between inner and peripheral nuclear matrix in regulation of chromatin
348 structures. For instance, in contrast to our findings that depletion of lamin B1 promotes
349 chromatin decompaction and relocalization from nuclear periphery to nucleoplasm, loss of
350 HNRNPU promotes global condensation of chromatin and increases lamina-associated
351 genomic regions. Moreover, genes enriched in cell adhesion are up-regulated in HNRNPU
352 depleted cells but down-regulated in lamin B1 knockout cells (fig. S7). At the A/B
353 compartment level, depletion of HNRNPU and lamin B1 both result in ~10% transition
354 between A/B compartments. Therefore, these two studies demonstrate that the inner and
355 peripheral nuclear matrix, through anchoring of chromatin in the nucleoplasm and the
356 nuclear envelop respectively, may offer a complementary, tug-of-war regulation of higher-
357 order chromatin organization.

358 In this work, we combined imaging and Hi-C sequencing to study the role of lamin
359 B1 in chromatin architecture and dynamics. We found that lamin B1 contributes to
360 segregation of chromosome territories and A/B compartments, and loss of lamin B1 leads

361 to chromatin decompaction and relocalization from nuclear periphery to nuclear interior.
362 Besides, loss of lamin B1 changes the location preference of genomic loci and increases
363 chromatin dynamics. Disruption of interactions between lamin B1 and DNA using
364 truncated lamin B1 leads to similar effects on chromatin dynamics caused by loss of lamin
365 B1. Dynamics of the same genomic locus is found to be correlated with its nuclear spatial
366 environment in that genomic sites close to the lamina are generally less mobile than those
367 localized in the nuclear interior. Our study demonstrates that it is chromatin decompaction
368 that mediates the effect of lamin B1 depletion on chromatin dynamics. Furthermore, our
369 study reveals that genomic loci in less compact compartment A are of higher mobility than
370 those in more compact compartment B. Taken together, our work supports lamin B1 plays
371 a crucial role in chromatin higher-order structure and chromatin dynamics.

372 **Materials and Methods**

373 **Construction of sgRNA expression plasmids and SunTag PiggyBac plasmids**

374 The mining process for repeats was similar as described recently(62). Briefly, the human
375 genome sequence was downloaded from the UCSC genome browser
376 (<http://genome.ucsc.edu>) with undetermined regions “Ns” replaced by randomly
377 generated nucleotides “A”, “T”, “G”, or “C”. Then the sequence was input to the Tandem
378 Repeat Finder bioinformatics tool (<http://tandem.bu.edu/trf/trf.html>) to identify the
379 tandem repeats. Highly conserved repeats with little mutation, proper repeat unit length
380 and repeat number were selected as candidates for live cell fluorescent labeling and
381 imaging. sgRNA oligoes targeting each repeat were designed upstream of proto-spacer
382 adjacent motif (PAM) sequence “NGG”. The oligoes of each sgRNA that target the
383 repeat regions on human chromosomes were synthesized by Beijing Ruibo biotech

384 (Beijing, China) with a 4 bp overhang flanking the sense and antisense strands. The
385 sgRNAs targeting lamin B1 gene were designed by the online tool Optimized CRISPR
386 Design (<http://crispr.mit.edu>) and candidates with the highest score were selected. The
387 sgRNA expression vector for imaging was based on the psgRNA2.0 transient expression
388 plasmid with an A-U flip and stem-loop extension (a gift from Prof. Wensheng Wei,
389 Peking University), containing the ccdB screening gene between two BsmBI sites for
390 inserting guide sequences into the sgRNAs. The sgRNA expression vector for editing
391 was based on plasmid pX330-U6-Chimeric_BB-CBh-hSpCas9 (Addgene Plasmid #
392 42230), containing two BpiI restriction sites for inserting guide sequences into the
393 sgRNAs. The targeting sgRNA expression plasmids were made by replacing the lethal
394 gene ccdB with annealed oligo using Golden Gate cloning with enzyme BsmBI and T4
395 ligase (NEB). For the sequence of each sgRNA construct.

396 In order to construct a stable cell line, the NLS_{SV40}-dCas9-3X NLS_{SV40}-24X GCN4-V4-
397 NLS_{SV40}-P2A-BFP fragment was amplified by PCR from plasmid pHRdSV40-NLS-
398 dCas9-24xGCN4_v4-NLS-P2A-BFP-dWPRE (Addgene Plasmid #60910) and then
399 ligated into PiggyBac plasmid pB-TRE3G-BsmBI-EF1 α -PuroR-P2A-rtTA by Golden
400 Gate Assembly with enzyme BsmBI and T4 ligase (NEB). The ScFV-sfGFP-GB1-
401 NLS_{SV40} fragment was amplified by PCR from plasmid pHR-scFv-GCN4-sfGFP-GB1-
402 NLS-dWPRE (Addgene Plasmid # 60906) and then ligated into PiggyBac plasmid pB-
403 TRE3G-BsmBI-EF1 α -HygroR-P2A-rtTA by Golden Gate Assembly with enzyme
404 BsmBI and T4 ligase (NEB).

405 **Cell culture, transfection and TSA treatment**

406 Human cell line MDA-MB-231 cells were maintained in Dulbecco's modified Eagle
407 medium with high glucose (Lifetech). The medium contained 10% Fetal bovine serum
408 (FBS) (Lifetech), and 1% of penicillin and streptomycin antibiotics (Lifetech). Cells were
409 maintained at 37 °C and 5% CO₂ in a humidified incubator. All plasmids were
410 transfected with Chemifect (Beijing Fengrui Biotech, Beijing, China) in accordance with
411 the manufacturer's protocol. TSA (TricostatinA, Sigma-Aldrich) was eluted to 3 mM in
412 DMSO. Cells were treated with 300 nM of TSA solution in complete growth medium for
413 24 hr before imaging experiments and the negative control sample was treated with
414 DMSO.

415 **CRISPR-mediated lamin B1 gene knockout**

416 In order to knockout lamin B1 genes, the cells were co-transfected with corresponding
417 sgRNA and Cas9 chimeric plasmid and an empty mCherry expressing plasmid. At 48 h
418 post transfection, cells were subjected to FACS to isolate mCherry positive single cell
419 clone in 96-well plates. After incubation for about a month, genome of each grown clone
420 was extracted and PCR-amplified with lamin B1-specific primer and sent for Sanger
421 sequencing. Clones with indel were verified by Western Blot and immunofluorescence.

422 **Construction of the SunTag stable cell line**

423 To construct the stable cell line, MDA-MB-231 cells were spread onto a 6-well plate one
424 day before transfection. On the next day, the cells were transfected with 500 ng pB-
425 TRE3G- NLS_{SV40}-dCas9-3X NLS_{SV40}-24X GCN4-_{v4}-NLS_{SV40}-P2A-BFP-PuroR-P2A-
426 rtTA, 500 ng pB-TRE3G-ScFV-sfGFP-GB1-NLS_{SV40}-HygroR-P2A-rtTA, and 200 ng
427 pCAG-hyPBase using Chemifect. After 48 hr, cells were subjected to hygromycin (200

428 $\mu\text{g/ml}$) and puromycin ($5 \mu\text{g/ml}$) selection. After incubation for two weeks, cells with
429 appropriate expression level of BFP and GFP were selected using FACS. Single cell
430 clones were harvested for imaging a month later.

431 **Immunofluorescence**

432 Cells were grown on 35mm glass bottom dish. After the coverage of cells reached 60-
433 70%, cells were fixed with 4% PFA for 15 min, permeabilized with 0.5% Triton in PBS
434 for 5 min and then blocked in blocking buffer containing 5% BSA and 0.1% Triton for 30
435 min. The cells were then incubated with primary antibodies in blocking buffer for 1 hr at
436 room temperature, washed with PBS three times, and then stained with organic dyes-
437 labeled secondary antibodies in blocking buffer for 1 hr at room temperature. The labeled
438 cells were washed again with PBS, then post-fixed with 4% PFA for 10 min and finally
439 stained with DAPI (Invitrogen).

440 Primary antibodies used in this study were lamin A/C (ab40467, Abcam, dilution 1:200),
441 lamin B1 (sc6216, Santa Cruz, dilution 1:200). Secondary antibodies were donkey anti-
442 rabbit Alexa Fluor 555 (A-31572, Thermo Fisher Scientific), donkey anti-goat Cy5 (705-
443 005-147, Jackson Immuno Research Laboratories, dilution 1:50), donkey anti-mouse
444 Cy3b (715-005-151, Jackson Immuno Research Laboratories, dilution 1:50).

445 **Optical setup and image acquisition**

446 Briefly, all tracking experiments in living cells were performed on an Olympus IX83
447 inverted microscope equipped with a $100\times$ UPlanSApo, N.A. 1.40, oil-immersion phase
448 objective and EMCCD (DU-897U-CS0-#BV). The microscope stage incubation chamber
449 was maintained at 37°C and 5% CO_2 . A 488-nm laser (2RU-VFL-P-300-488-B1R;

450 MPB) was used to excite the sfGFP fluorophore. The laser power was modulated by
451 anacousto-optic-tunable-filtre (AOTF) and the beam width was expanded fivefold and
452 focused at the back focal plane of the objective. The power density at the sample, with
453 epifluorescence illumination, was 10 μ W at 488nm. The microscope was controlled by
454 home-written scripts. Movies of chromatin dynamics in living cells were acquired at 10
455 Hz. The motions of loci were studied by recording their trajectories in 2D rather than in
456 3D to increase time resolution and reduce phototoxicity. According to previous study,
457 there is no significant difference in the movement volumes and diffusion coefficient of
458 telomeres between different cell cycle stages in interphase, thus we collected images in
459 interphase without further distinguishing between sub-stages of interphase.

460 For fixed cell conventional imaging experiments, an UltraVIEW VoX spinning disc
461 microscope (PerkinElmer) was used. STORM imaging of lamin B1 was done on N-
462 STORM (Nikon, Japan)

463 **Image analysis**

464 All image stacks were analyzed using MATLAB tracking package ‘U-track’. Fluorescent
465 puncta were identified in each frame with 2D Gaussian fitting after Fourier low-pass
466 filtering. The coordinates of the fluorescent puncta were determined. Trajectories were
467 created by linking identified puncta to their nearest neighbor within a maximum distance
468 range of 5 camera pixels (800 nm) in the previous frame. Particles with trajectory gap
469 larger than 10 consecutive frames were treated as two particles.

470 For each trajectory, the mean square displacement (MSD) as a function of time delay was
471 calculated by the following equation :

$$\begin{aligned} 472 \quad MSD(n\delta t) &= \frac{1}{N-1-n} \sum_{j=1}^{N-1-n} \{[x(j\delta t + n\delta t) - x(j\delta t)]^2 \\ 473 \quad &+ [y(j\delta t + n\delta t) - y(j\delta t)]^2\} \end{aligned}$$

474 where δt is the time interval between two successive frames, $x(t)$ and $y(t)$ are the
475 coordinates at time t , N is the total number of frames, and n is the number of time
476 intervals. To maximize precision in long-range MSD, intervals smaller than $N/10$ were
477 used for the calculation.

478 The analysis of MSD curves was carried out using custom MATLAB scripts. Each
479 individual MSD curve was fitted by least-squares regression to the following model:

$$480 \quad MSD = Dt^\alpha$$

481 where D is the diffusion coefficient and α is the scaling factor. For each repeat, many
482 trajectories were fitted and grouped. Additionally, every collected cell was inspected
483 carefully, and any cell with slight motion was discarded to eliminate the contamination of
484 such drift in the analysis of loci trajectories.

485 The three-dimensional image analysis was carried out in Imaris (Bitplane) by ImarisCell,
486 a module designed specifically to identify, segment, track, measure and analyze cell,
487 nucleus and vesicles in 3D images. Using “Cell Boundary from Cytoplasm” function, the
488 nucleus was segmented by DAPI channel as the nuclear boundary and the genomic loci
489 were fitted with 3D ellipsoid function as a spot. Then the shortest distance between the
490 spot and the surface was calculated. For chromosome painting image analysis, “Surface”
491 function was used to segment nuclear boundary by DAPI channel and territory boundary
492 of chromosome 2 and chromosome 18 by 488 nm and 561 nm channel intensity. The

493 volume and center of mass of nucleus and chromosome territories were output directly.
494 The volume of each nucleus was measured to normalize the volume of chromosome
495 territories. Distance between nuclear center of mass and chromosome territories was
496 normalized by the cubic root of nuclear volume.

497 The threshold for subnuclear position assignment of loci was as follows: 4 pixels'
498 distance between the locus and nuclear envelope (640 nm), referring to previous
499 publication about LMNB1 LAD FISH analysis (defined there as < 700nm, or 8 pixels,
500 from the nucleus edge)(63).

501 STORM original data was processed by Insight3, ImageJ, and finally reconstructed to an
502 image by home-written MATLAB scripts(64).

503 **Western blot**

504 The cell lysates were blotted against the following primary antibodies: lamin B1 (sc6216,
505 Santa Cruz, dilution 1:500) and β -actin (sc47778, Santa Cruz, dilution 1:500). The blots
506 were visualized with peroxidase-coupled secondary antibodies.

507 **PI staining**

508 Cells grown on 60 mm dish were digested by trypsin and collected to 1.5 ml tube. After
509 being washed with PBS twice, cells were fixed in pre-chilled 75% ethanol at -20°C
510 overnight. The fixed cells were washed to remove ethanol, and then incubated in solution
511 of 100 $\mu\text{g/ml}$ RNase A and 0.2% Triton X-100 for 30 min at 37°C . Subsequent
512 centrifugation of the samples was followed by a wash in PBS and staining with PI

513 solution (50 µg/ml PI, 0.2% Triton X-100) at room temperature for 30 min. Cells stained
514 with PI were analyzed in Flow cytometer (BD LSRFortessa™) directly(65).

515 **Chromosome painting**

516 Cells were grown on 22 x 22 mm² coverslips. After the coverage of cells reached 70-
517 80%, cells were fixed at -20 °C for 20 min in a pre-chilled solution of methanol and
518 acetic acid at 3:1 ratio and then treated with 10 µl of probe mix with 5 µl of each probe.
519 The probe mix immersed cells were covered with a glass slide (25 x 75 mm) and sealed
520 with rubber cement. The sample and probe were denatured simultaneously by heating
521 slide on a hotplate at 75 °C for 2 min and incubated in a humidified chamber at 37 °C
522 overnight. The coverslip was removed carefully from slide, washed in 0.4 x SSC at 72 °C
523 for 2 min, and then in 2 x SSC, 0.05% Tween-20 at room temperature for 30 seconds.
524 The labeled cells were rinsed briefly in PBS and finally mounted with ProLong®
525 Diamond Antifade Mountant with DAPI (P36962, Thermo Fisher Scientific).
526 Chromosome 2 painting probe mix was XCP 2 green (D-0302-100-FI XCP 2,
527 Metasystems) and Chromosome 18 painting probe mix was XCP 18 orange (D-0318-
528 100-OR XCP 18, Metasystems).

529 **Hi-C experiment**

530 Hi-C experiment was performed following the in situ Hi-C protocol(46). Briefly, cells
531 were grown to about 70-80 % confluence, washed with PBS, crosslinked with 1%, v/v
532 formaldehyde solution, and the reaction was quenched by 0.2M glycine solution. Cells
533 were lysed and DNA was then cut with MboI and the overhangs were filled with a

534 biotinylated base. Free ends were then ligated together in situ. Crosslinks were reversed,
535 the DNA was sheared to 300-500bp and then biotinylated ligation junctions were
536 recovered with streptavidin beads.

537 Sequencing libraries were generated using standard Illumina library construction
538 protocol. Briefly, ends of sheared DNA were repaired and the blunt ends were added an
539 “A” base to ligate with Illumina's adapters that have a single 'T' base overhang. Then
540 DNA was PCR amplified for 8-12 cycles. At last, products were purified using AMPure
541 XP system and sequenced through XTen (Illumina).

542 **Hi-C data analysis**

543 Hi-C data analysis was performed with HiC-Pro(66). Briefly, reads were first aligned on
544 the hg19 reference genome. Uniquely mapped reads were assigned to restriction
545 fragments. Then the invalid ligation products were filtered out, and eligible read pairs
546 were counted to build Hi-C contact maps. At last, ICE normalization(67) was used to
547 normalize the raw counts data.

548 Compartment A/B analysis. ICE-normalized 500-kb resolution matrices were used to
549 detect chromatin compartments by R package HiTC(68). The whole genome was divided
550 into two compartments based on the positive or negative values of the first principal
551 component. The part with higher gene density was assigned as compartment A and the
552 other part as compartment B.

553 TAD analysis. ICE-normalized 40-kb resolution matrices were used to detect TAD by
554 Perl script matrix2insulation.pl (<http://github.com/blajoie/crane-nature-2015>). Insulation
555 scores were calculated for each 40-kb bin, and the valleys of insulation score curves were

556 defined as TAD boundaries. TADs smaller than 200 kb were filtered out as in previous
557 method(51).

558 **Supplementary Materials**

559 Supplementary material for this article is available at

560 Fig. S1. Preparation of lamin B1 knock-out (KO) cell lines.

561 Fig. S2. Reproducibility analysis of Hi-C data.

562 Fig. S3. TAD analysis

563 Fig. S4. Construction of SunTag stable cell line, comparison between 2D and 3D images
564 and description of lamin B1 truncation.

565 Fig. S5. MSD curves of 1Mb loci on chromosome 2.

566 Fig. S6. Model.

567 Fig. S7. GO (Biological Process) analysis of down-regulated genes upon lamin B1 KO.

568 Table S1. Quality control statistics for Hi-C data processing.

569 Movie. A representative movie and tracking trajectory of labeled genomic locus in a
570 living cell.

571 **References and Notes**

- 572 1. A. N. Boettiger, B. Bintu, J. R. Moffitt, S. Wang, B. J. Beliveau, G. Fudenberg, M. Imakaev,
573 L. A. Mirny, C. T. Wu, X. Zhuang, Super-resolution imaging reveals distinct chromatin
574 folding for different epigenetic states. *Nature* **529**, 418-422 (2016).
- 575 2. S. Wang, J. H. Su, B. J. Beliveau, B. Bintu, J. R. Moffitt, C. T. Wu, X. Zhuang, Spatial
576 organization of chromatin domains and compartments in single chromosomes. *Science*
577 **353**, 598-602 (2016).

- 578 3. B. Bintu, L. J. Mateo, J.-H. Su, N. A. Sinnott-Armstrong, M. Parker, S. Kinrot, K. Yamaya,
579 A. N. Boettiger, X. Zhuang, Super-resolution chromatin tracing reveals domains and
580 cooperative interactions in single cells. *Science* **362**, eaau1783 (2018).
- 581 4. J. Dekker, K. Rippe, M. Dekker, N. Kleckner, Capturing chromosome conformation.
582 *Science* **295**, 1306-1311 (2002).
- 583 5. M. Simonis, P. Klous, E. Splinter, Y. Moshkin, R. Willemsen, E. de Wit, B. van Steensel, W.
584 de Laat, Nuclear organization of active and inactive chromatin domains uncovered by
585 chromosome conformation capture-on-chip (4C). *Nat. Genet.* **38**, 1348-1354 (2006).
- 586 6. J. Dostie, T. A. Richmond, R. A. Arnaout, R. R. Selzer, W. L. Lee, T. A. Honan, E. D. Rubio,
587 A. Krumm, J. Lamb, C. Nusbaum, R. D. Green, J. Dekker, Chromosome Conformation
588 Capture Carbon Copy (5C): a massively parallel solution for mapping interactions
589 between genomic elements. *Genome Res.* **16**, 1299-1309 (2006).
- 590 7. E. Lieberman-Aiden, N. L. van Berkum, L. Williams, M. Imakaev, T. Ragozy, A. Telling, I.
591 Amit, B. R. Lajoie, P. J. Sabo, M. O. Dorschner, R. Sandstrom, B. Bernstein, M. A. Bender,
592 M. Groudine, A. Gnirke, J. Stamatoyannopoulos, L. A. Mirny, E. S. Lander, J. Dekker,
593 Comprehensive mapping of long-range interactions reveals folding principles of the
594 human genome. *Science* **326**, 289-293 (2009).
- 595 8. M. J. Fullwood, M. H. Liu, Y. F. Pan, J. Liu, H. Xu, Y. B. Mohamed, Y. L. Orlov, S. Velkov, A.
596 Ho, P. H. Mei, E. G. Y. Chew, P. Y. H. Huang, W.-J. Welboren, Y. Han, H. S. Ooi, P. N.
597 Ariyaratne, V. B. Vega, Y. Luo, P. Y. Tan, P. Y. Choy, K. D. S. A. Wansa, B. Zhao, K. S. Lim,
598 S. C. Leow, J. S. Yow, R. Joseph, H. Li, K. V. Desai, J. S. Thomsen, Y. K. Lee, R. K. M.
599 Karuturi, T. Herve, G. Bourque, H. G. Stunnenberg, X. Ruan, V. Cacheux-Rataboul, W.-K.
600 Sung, E. T. Liu, C.-L. Wei, E. Cheung, Y. Ruan, An oestrogen-receptor- α -bound human
601 chromatin interactome. *Nature* **462**, 58-64 (2009).
- 602 9. T. Nagano, Y. Lubling, T. J. Stevens, S. Schoenfelder, E. Yaffe, W. Dean, E. D. Laue, A.
603 Tanay, P. Fraser, Single-cell Hi-C reveals cell-to-cell variability in chromosome structure.
604 *Nature* **502**, 59-64 (2013).
- 605 10. E. P. Nora, A. Goloborodko, A. L. Valton, J. H. Gibcus, A. Uebersohn, N. Abdennur, J.
606 Dekker, L. A. Mirny, B. G. Bruneau, Targeted Degradation of CTCF Decouples Local
607 Insulation of Chromosome Domains from Genomic Compartmentalization. *Cell* **169**, 930-
608 944 e922 (2017).
- 609 11. G. Wutz, C. Várnai, K. Nagasaka, D. A. Cisneros, R. R. Stocsits, W. Tang, S. Schoenfelder,
610 G. Jessberger, M. Muhar, M. J. Hossain, N. Walther, B. Koch, M. Kueblbeck, J. Ellenberg,
611 J. Zuber, P. Fraser, J. M. Peters, Topologically associating domains and chromatin loops
612 depend on cohesin and are regulated by CTCF, WAPL, and PDS5 proteins. *The EMBO*
613 *Journal* **36**, 3573-3599 (2017).
- 614 12. S. S. P. Rao, S. C. Huang, B. Glenn St Hilaire, J. M. Engreitz, E. M. Perez, K. R. Kieffer-
615 Kwon, A. L. Sanborn, S. E. Johnstone, G. D. Bascom, I. D. Bochkov, X. Huang, M. S.
616 Shamim, J. Shin, D. Turner, Z. Ye, A. D. Omer, J. T. Robinson, T. Schlick, B. E. Bernstein, R.
617 Casellas, E. S. Lander, E. L. Aiden, Cohesin Loss Eliminates All Loop Domains. *Cell* **171**,
618 305-320 e324 (2017).
- 619 13. W. Schwarzer, N. Abdennur, A. Goloborodko, A. Pekowska, G. Fudenberg, Y. Loe-Mie, N.
620 A. Fonseca, W. Huber, H. H. C, L. Mirny, F. Spitz, Two independent modes of chromatin
621 organization revealed by cohesin removal. *Nature* **551**, 51-56 (2017).
- 622 14. J. H. I. Haarhuis, R. H. van der Weide, V. A. Blomen, J. O. Yanez-Cuna, M. Amendola, M.
623 S. van Ruiten, P. H. L. Krijger, H. Teunissen, R. H. Medema, B. van Steensel, T. R.
624 Brummelkamp, E. de Wit, B. D. Rowland, The Cohesin Release Factor WAPL Restricts
625 Chromatin Loop Extension. *Cell* **169**, 693-707 e614 (2017).

- 626 15. J. Nuebler, G. Fudenberg, M. Imakaev, N. Abdennur, L. A. Mirny, Chromatin organization
627 by an interplay of loop extrusion and compartmental segregation. *Proc. Natl. Acad. Sci.*
628 *U. S. A.* **115**, E6697-E6706 (2018).
- 629 16. B. van Steensel, A. S. Belmont, Lamina-Associated Domains: Links with Chromosome
630 Architecture, Heterochromatin, and Gene Repression. *Cell* **169**, 780-791 (2017).
- 631 17. I. Solovei, K. Thanisch, Y. Feodorova, How to rule the nucleus: divide et impera. *Curr.*
632 *Opin. Cell Biol.* **40**, 47-59 (2016).
- 633 18. H. B. Sun, J. Shen, H. Yokota, Size-Dependent Positioning of Human Chromosomes in
634 Interphase Nuclei. *Biophys. J.* **79**, 184-190 (2000).
- 635 19. X. Zheng, J. Hu, S. Yue, L. Kristiani, M. Kim, M. Sauria, J. Taylor, Y. Kim, Y. Zheng, Lamins
636 Organize the Global Three-Dimensional Genome from the Nuclear Periphery. *Mol. Cell*
637 **71**, 802-815 e807 (2018).
- 638 20. N. Briand, P. Collas, Laminopathy-causing lamin A mutations reconfigure lamina-
639 associated domains and local spatial chromatin conformation. *Nucleus* **9**, 216-226
640 (2018).
- 641 21. T. R. Luperchio, M. E. Sauria, X. Wong, M.-C. Gaillard, P. Tsang, K. Pekrun, R. A. Ach, N. A.
642 Yamada, J. Taylor, K. Reddy, Chromosome Conformation Paints Reveal The Role Of
643 Lamina Association In Genome Organization And Regulation. *bioRxiv*, 122226 (2017).
- 644 22. S. Shao, B. Xue, Y. Sun, Intranucleus Single-Molecule Imaging in Living Cells. *Biophys J*
645 **115**, 181-189 (2018).
- 646 23. C. H. Chuang, A. E. Carpenter, B. Fuchsova, T. Johnson, P. de Lanerolle, A. S. Belmont,
647 Long-range directional movement of an interphase chromosome site. *Curr. Biol.* **16**, 825-
648 831 (2006).
- 649 24. H. Ochiai, T. Sugawara, T. Yamamoto, Simultaneous live imaging of the transcription and
650 nuclear position of specific genes. *Nucleic Acids Res.* **43**, e127 (2015).
- 651 25. N. Dimitrova, Y.-C. M. Chen, D. L. Spector, T. de Lange, 53BP1 promotes non-
652 homologous end joining of telomeres by increasing chromatin mobility. *Nature* **456**,
653 524-528 (2008).
- 654 26. N. W. Cho, R. L. Dilley, M. A. Lampson, R. A. Greenberg, Interchromosomal homology
655 searches drive directional ALT telomere movement and synapsis. *Cell* **159**, 108-121
656 (2014).
- 657 27. B. Gu, T. Swigut, A. Spencley, M. R. Bauer, M. Chung, T. Meyer, J. Wysocka,
658 Transcription-coupled changes in nuclear mobility of mammalian cis-regulatory
659 elements. *Science* **359**, 1050-1055 (2018).
- 660 28. P. H. Viollier, M. Thanbichler, P. T. McGrath, L. West, M. Meewan, H. H. McAdams, L.
661 Shapiro, Rapid and sequential movement of individual chromosomal loci to specific
662 subcellular locations during bacterial DNA replication. *Proc. Natl. Acad. Sci. U. S. A.* **101**,
663 9257-9262 (2004).
- 664 29. A. Javer, Z. Long, E. Nugent, M. Grisi, K. Siriwatwetchakul, K. D. Dorfman, P. Cicuta, M.
665 Cosentino Lagomarsino, Short-time movement of E. coli chromosomal loci depends on
666 coordinate and subcellular localization. *Nat. Commun.* **4**, 3003 (2013).
- 667 30. H. Hajjoul, J. Mathon, H. Ranchon, I. Goiffon, J. Mozziconacci, B. Albert, P. Carrivain, J.
668 M. Victor, O. Gadal, K. Bystricky, A. Bancaud, High-throughput chromatin motion
669 tracking in living yeast reveals the flexibility of the fiber throughout the genome.
670 *Genome Res.* **23**, 1829-1838 (2013).
- 671 31. K. D. Kim, H. Tanizawa, O. Iwasaki, C. J. Corcoran, J. R. Capizzi, J. E. Hayden, K. Noma,
672 Centromeric motion facilitates the mobility of interphase genomic regions in fission
673 yeast. *J. Cell Sci.* **126**, 5271-5283 (2013).

- 674 32. B. Albert, J. Mathon, A. Shukla, H. Saad, C. Normand, I. Leger-Silvestre, D. Villa, A.
675 Kamgoue, J. Mozziconacci, H. Wong, C. Zimmer, P. Bhargava, A. Bancaud, O. Gadal,
676 Systematic characterization of the conformation and dynamics of budding yeast
677 chromosome XII. *J. Cell Biol.* **202**, 201-210 (2013).
- 678 33. J. S. Verdaasdonk, P. A. Vasquez, R. M. Barry, T. Barry, S. Goodwin, M. G. Forest, K.
679 Bloom, Centromere tethering confines chromosome domains. *Mol. Cell* **52**, 819-831
680 (2013).
- 681 34. M. R. Hubner, D. L. Spector, Chromatin dynamics. *Annu. Rev. Biophys.* **39**, 471-489
682 (2010).
- 683 35. J. R. Chubb, S. Boyle, P. Perry, W. A. Bickmore, Chromatin motion is constrained by
684 association with nuclear compartments in human cells. *Curr. Biol.* **12**, 439-445 (2002).
- 685 36. I. Bronshtein, E. Kepten, I. Kanter, S. Berezin, M. Lindner, A. B. Redwood, S. Mai, S.
686 Gonzalo, R. Foisner, Y. Shav-Tal, Y. Garini, Loss of lamin A function increases chromatin
687 dynamics in the nuclear interior. *Nat. Commun.* **6**, 8044 (2015).
- 688 37. T. Shimi, K. Pflieger, S. Kojima, C. G. Pack, I. Solovei, A. E. Goldman, S. A. Adam, D. K.
689 Shumaker, M. Kinjo, T. Cremer, R. D. Goldman, The A- and B-type nuclear lamin
690 networks: microdomains involved in chromatin organization and transcription. *Genes*
691 *Dev.* **22**, 3409-3421 (2008).
- 692 38. K. Gesson, P. Rescheneder, M. P. Skoruppa, A. von Haeseler, T. Dechat, R. Foisner, A-
693 type lamins bind both hetero- and euchromatin, the latter being regulated by lamina-
694 associated polypeptide 2 alpha. *Genome Res.* **26**, 462-473 (2016).
- 695 39. W. Meuleman, D. Peric-Hupkes, J. Kind, J.-B. Beaudry, L. Pagie, M. Kellis, M. Reinders, L.
696 Wessels, B. van Steensel, Constitutive nuclear lamina-genome interactions are highly
697 conserved and associated with A/T-rich sequence. *Genome Res.* **23**, 270-280 (2013).
- 698 40. Y. Gruenbaum, R. Foisner, Lamins: nuclear intermediate filament proteins with
699 fundamental functions in nuclear mechanics and genome regulation. *Annu. Rev.*
700 *Biochem.* **84**, 131-164 (2015).
- 701 41. C. Uhler, G. V. Shivashankar, Regulation of genome organization and gene expression by
702 nuclear mechanotransduction. *Nat. Rev. Mol. Cell Biol.* **18**, 717-727 (2017).
- 703 42. C. Y. Ho, J. Lammerding, Lamins at a glance. *J. Cell Sci.* **125**, 2087-2093 (2012).
- 704 43. J. A. Croft, J. M. Bridger, S. Boyle, P. Perry, P. Teague, W. A. Bickmore, Differences in the
705 Localization and Morphology of Chromosomes in the Human Nucleus. *The Journal of Cell*
706 *Biology* **145**, 1119-1131 (1999).
- 707 44. J. Kind, L. Pagie, S. S. de Vries, L. Nahidiazar, S. S. Dey, M. Bienko, Y. Zhan, B. Lajoie, C. A.
708 de Graaf, M. Amendola, G. Fudenberg, M. Imakaev, L. A. Mirny, K. Jalink, J. Dekker, A.
709 van Oudenaarden, B. van Steensel, Genome-wide maps of nuclear lamina interactions in
710 single human cells. *Cell* **163**, 134-147 (2015).
- 711 45. M. Cremer, K. Küpper, B. Wagler, L. Wizelman, J. von Hase, Y. Weiland, L. Kreja, J.
712 Diebold, M. R. Speicher, T. Cremer, Inheritance of gene density-related higher order
713 chromatin arrangements in normal and tumor cell nuclei. *The Journal of cell biology* **162**,
714 809-820 (2003).
- 715 46. S. S. Rao, M. H. Huntley, N. C. Durand, E. K. Stamenova, I. D. Bochkov, J. T. Robinson, A.
716 L. Sanborn, I. Machol, A. D. Omer, E. S. Lander, E. L. Aiden, A 3D map of the human
717 genome at kilobase resolution reveals principles of chromatin looping. *Cell* **159**, 1665-
718 1680 (2014).
- 719 47. P. G. Maass, A. R. Barutcu, C. L. Weiner, J. L. Rinn, Inter-chromosomal Contact Properties
720 in Live-Cell Imaging and in Hi-C. *Mol. Cell* **69**, 1039-1045 e1033 (2018).

- 721 48. Z. Du, H. Zheng, B. Huang, R. Ma, J. Wu, X. Zhang, J. He, Y. Xiang, Q. Wang, Y. Li, J. Ma, X.
722 Zhang, K. Zhang, Y. Wang, M. Q. Zhang, J. Gao, J. R. Dixon, X. Wang, J. Zeng, W. Xie,
723 Allelic reprogramming of 3D chromatin architecture during early mammalian
724 development. *Nature* **547**, 232-235 (2017).
- 725 49. E. P. Nora, B. R. Lajoie, E. G. Schulz, L. Giorgetti, I. Okamoto, N. Servant, T. Piolot, N. L.
726 van Berkum, J. Meisig, J. Sedat, J. Gribnau, E. Barillot, N. Bluthgen, J. Dekker, E. Heard,
727 Spatial partitioning of the regulatory landscape of the X-inactivation centre. *Nature* **485**,
728 381-385 (2012).
- 729 50. J. R. Dixon, S. Selvaraj, F. Yue, A. Kim, Y. Li, Y. Shen, M. Hu, J. S. Liu, B. Ren, Topological
730 domains in mammalian genomes identified by analysis of chromatin interactions.
731 *Nature* **485**, 376-380 (2012).
- 732 51. E. Crane, Q. Bian, R. P. McCord, B. R. Lajoie, B. S. Wheeler, E. J. Ralston, S. Uzawa, J.
733 Dekker, B. J. Meyer, Condensin-driven remodelling of X chromosome topology during
734 dosage compensation. *Nature* **523**, 240-244 (2015).
- 735 52. J. Ruan, C. Xu, C. Bian, R. Lam, J. P. Wang, J. Kania, J. Min, J. Zang, Crystal structures of
736 the coil 2B fragment and the globular tail domain of human lamin B1. *FEBS Lett.* **586**,
737 314-318 (2012).
- 738 53. Y. B. Luo, F. L. Mastaglia, S. D. Wilton, Normal and aberrant splicing of LMNA. *J. Med.*
739 *Genet.* **51**, 215-223 (2014).
- 740 54. M. Di Pierro, D. A. Potoyan, P. G. Wolynes, J. N. Onuchic, Anomalous diffusion, spatial
741 coherence, and viscoelasticity from the energy landscape of human chromosomes. *Proc.*
742 *Natl. Acad. Sci. U. S. A.* **115**, 7753-7758 (2018).
- 743 55. K. Jaqaman, D. Loerke, M. Mettlen, H. Kuwata, S. Grinstein, S. L. Schmid, G. Danuser,
744 Robust single-particle tracking in live-cell time-lapse sequences. *Nat. Methods* **5**, 695-
745 702 (2008).
- 746 56. M. A. Ricci, C. Manzo, M. F. Garcia-Parajo, M. Lakadamyali, M. P. Cosma, Chromatin
747 fibers are formed by heterogeneous groups of nucleosomes in vivo. *Cell* **160**, 1145-1158
748 (2015).
- 749 57. L. Liu, G. Shi, D. Thirumalai, C. Hyeon, Chain organization of human interphase
750 chromosome determines the spatiotemporal dynamics of chromatin loci. *PLoS Comp.*
751 *Biol.* **14**, e1006617 (2018).
- 752 58. M. Falk, Y. Feodorova, N. Naumova, M. Imakaev, B. R. Lajoie, H. Leonhardt, B. Joffe, J.
753 Dekker, G. Fudenberg, I. Solovei, L. Mirny, Heterochromatin drives organization of
754 conventional and inverted nuclei. *bioRxiv*, 244038 (2018).
- 755 59. I. Solovei, A. S. Wang, K. Thanisch, C. S. Schmidt, S. Krebs, M. Zwerger, T. V. Cohen, D.
756 Devys, R. Foisner, L. Peichl, H. Herrmann, H. Blum, D. Engelkamp, C. L. Stewart, H.
757 Leonhardt, B. Joffe, LBR and lamin A/C sequentially tether peripheral heterochromatin
758 and inversely regulate differentiation. *Cell* **152**, 584-598 (2013).
- 759 60. J. Camps, D. Wangsa, M. Falke, M. Brown, C. M. Case, M. R. Erdos, T. Ried, Loss of lamin
760 B1 results in prolongation of S phase and decondensation of chromosome territories.
761 *FASEB J.* **28**, 3423-3434 (2014).
- 762 61. H. Fan, P. Lv, X. Huo, J. Wu, Q. Wang, L. Cheng, Y. Liu, Q. Q. Tang, L. Zhang, F. Zhang, X.
763 Zheng, H. Wu, B. Wen, The nuclear matrix protein HNRNPU maintains 3D genome
764 architecture globally in mouse hepatocytes. *Genome Res.* **28**, 192-202 (2018).
- 765 62. H. Ma, A. Naseri, P. Reyes-Gutierrez, S. A. Wolfe, S. Zhang, T. Pederson, Multicolor
766 CRISPR labeling of chromosomal loci in human cells. *Proc. Natl. Acad. Sci. U.S.A.* **112**,
767 3002-3007 (2015).

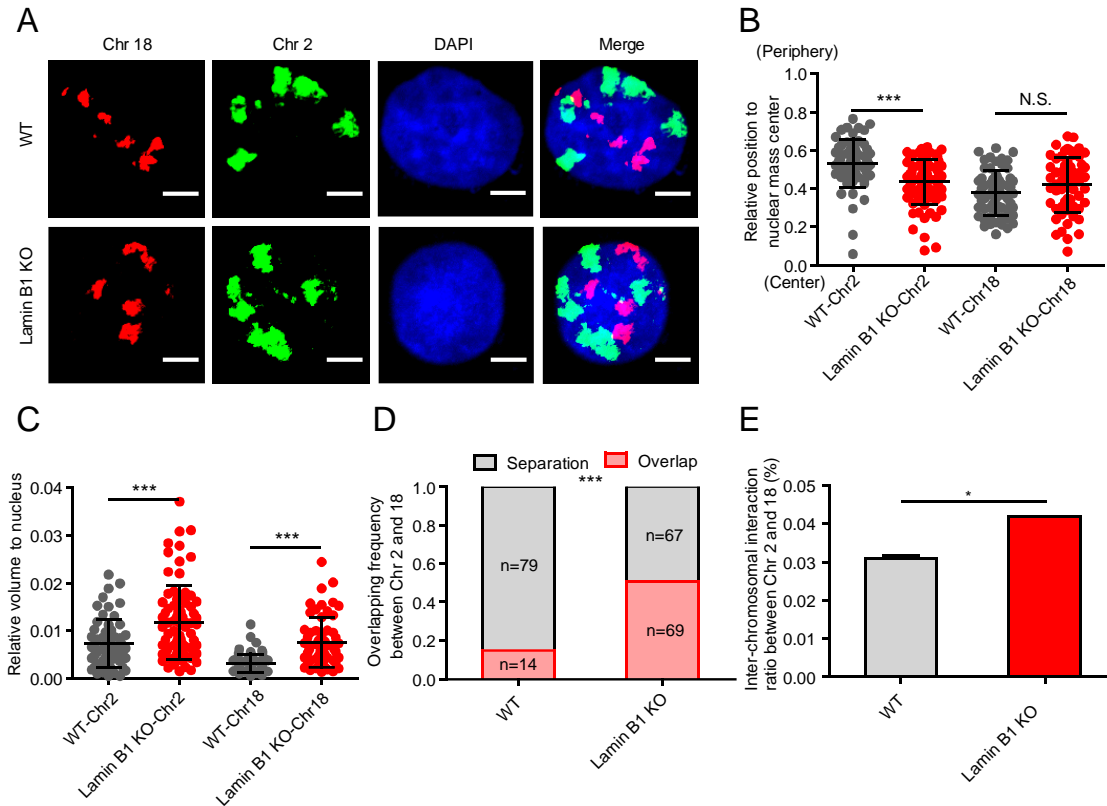
- 768 63. J. Kind, L. Pagie, H. Ortazokoyun, S. Boyle, Sandra S. de Vries, H. Janssen, M. Amendola,
769 Leisha D. Nolen, Wendy A. Bickmore, B. van Steensel, Single-Cell Dynamics of Genome-
770 Nuclear Lamina Interactions. *Cell* **153**, 178-192 (2013).
- 771 64. M. J. Rust, M. Bates, X. Zhuang, Sub-diffraction-limit imaging by stochastic optical
772 reconstruction microscopy (STORM). *Nat. Methods* **3**, 793-795 (2006).
- 773 65. A. Krishan, Rapid flow cytofluorometric analysis of mammalian cell cycle by propidium
774 iodide staining. *The Journal of Cell Biology* **66**, 188-193 (1975).
- 775 66. N. Servant, N. Varoquaux, B. R. Lajoie, E. Viara, C.-J. Chen, J.-P. Vert, E. Heard, J. Dekker,
776 E. Barillot, HiC-Pro: an optimized and flexible pipeline for Hi-C data processing. *Genome*
777 *Biol.* **16**, 259 (2015).
- 778 67. M. Imakaev, G. Fudenberg, R. P. McCord, N. Naumova, A. Goloborodko, B. R. Lajoie, J.
779 Dekker, L. A. Mirny, Iterative correction of Hi-C data reveals hallmarks of chromosome
780 organization. *Nat. Methods* **9**, 999-1003 (2012).
- 781 68. N. Servant, B. R. Lajoie, E. P. Nora, L. Giorgetti, C. J. Chen, E. Heard, J. Dekker, E. Barillot,
782 HiTC: exploration of high-throughput 'C' experiments. *Bioinformatics* **28**, 2843-2844
783 (2012).

784 **Acknowledgments**

785 **General:** We thank Dr. Ronald D. Vale (University of California, San Francisco) for
786 providing SunTag plasmids, Dr. Wensheng Wei (School of life sciences, Peking
787 University) for providing sgRNA expression plasmid, Dr. Feng Zhang (Broad Institute)
788 for providing plasmids px330 (Addgene Plasmid # 42230) and Dr. Wei Guo (Department
789 of Biology, University of Pennsylvania) for providing the MDA-MB-231 cell line. We
790 also thank Dr Hongxia Lv at the core imaging facility of the School of Life Sciences,
791 Peking University for imaging support. **Funding:** This work is supported by grants from
792 National Key R&D Program of China, No. 2017YFA0505302, the National Natural
793 Science Foundation of China 21573013, 21825401 for Y.S., and Chinese National Key
794 Projects of Research and Development, No. 2016YFA0100103, Peking-Tsinghua Center
795 for Life Sciences, and National Natural Science Foundation of China Key Research Grant
796 71532001 for C.L.. **Author contributions:** Y.S., C.L., L.C., and S.S. conceived and designed
797 the experiments. L.C. performed all the cloning, immunofluorescence, western blot, chromosome
798 painting, live cell tracking experiments and image data analysis. M.L. performed Hi-C

799 experiments and conducted data analysis of Hi-C and RNA-seq. S.S. wrote the MATLAB script
800 for images analysis and carried out the stable cell line construction and knockout experiments.
801 Y.H. gave help in FISH experiments. B.X. involved in the critical discussion. L.C., M.L., S.S.,
802 C.L., and Y.S. wrote the manuscript. **Competing interests:** The authors declare that they have no
803 competing interests.

804 **Figures**



805

806 **Fig. 1 Lamin B1 regulates chromatin sub-nuclear localization and global compaction**

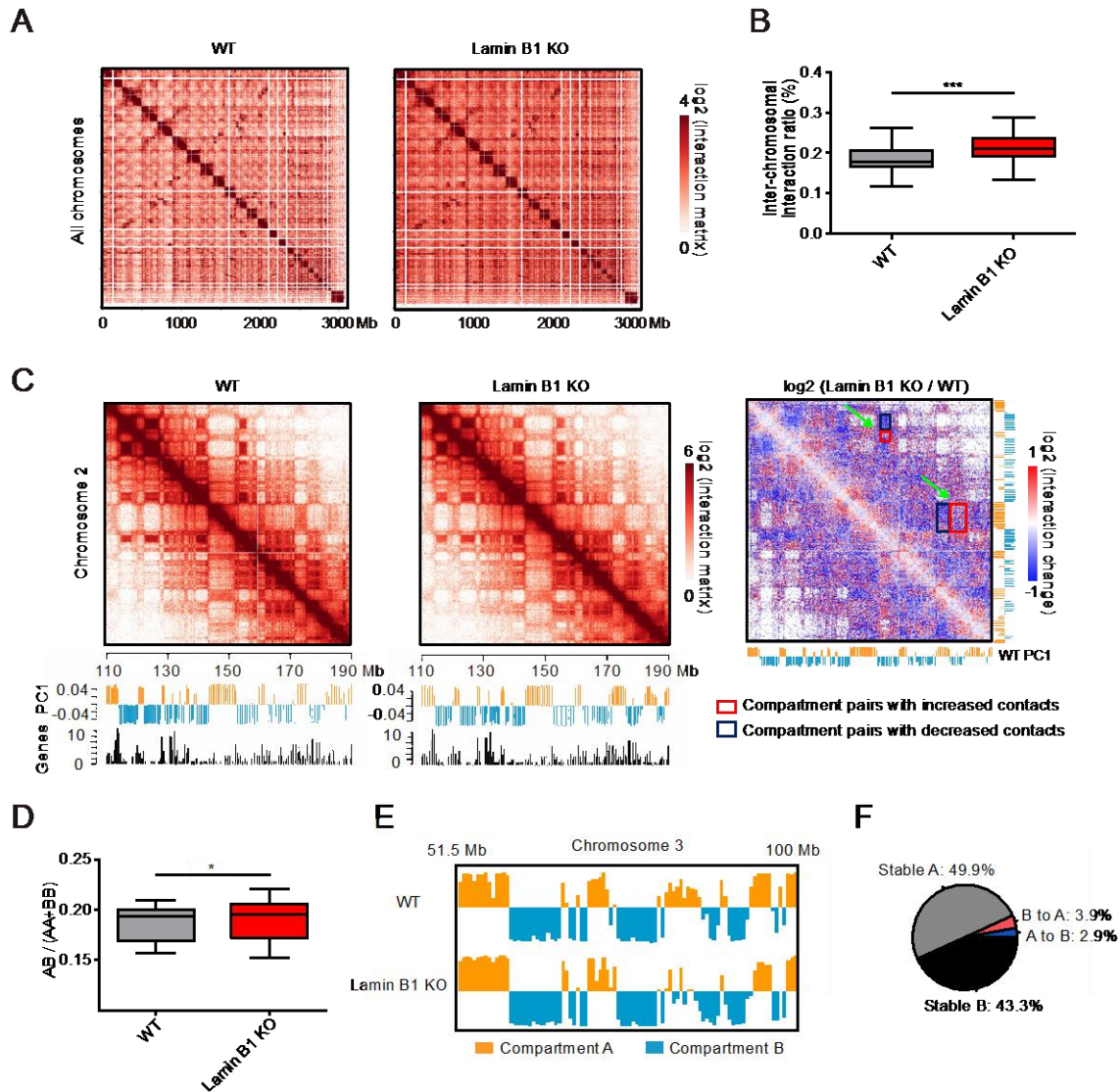
807 (A) Two representative three dimensional (3D)-projection chromosome painting images of
808 chromosome 2 and 18. Green: FISH signal of chromosome 2. Red: FISH signal of
809 chromosome 18. Blue: DAPI staining. The maximum intensity projections of nuclear Z
810 stacks are displayed. Scale bars, 5 μ m.

811 (B) Quantification of the nuclear localization of chromosomes based on their relative
812 distances from the chromosome mass center to the nuclear mass center. This distance is
813 normalized by the cubic root of the nuclear volume. Mean \pm standard deviation (SD). ***
814 $p < 0.001$, Mann–Whitney test. 3 independent experiments.

815 (C) Quantification of the volumes occupied by chromosome 2 and 18 relative to the nuclear
816 volume. Chromosomes in lamin B1-KO cells show significantly larger relative volumes.
817 Mean \pm SD. *** $p < 0.001$, Mann–Whitney test. 3 independent experiments.

818 (D) Quantification of the overlap frequency between chromosome 2 and chromosome 18
819 territories. The ratio of cells presenting territory interaction between chromosome 2 and
820 chromosome 18 in wild type (WT) cells is significantly smaller than that in lamin B1-KO
821 cells. *** $p < 0.001$, Fisher’s exact test. 3 independent experiments.

822 (E) Trans-interaction ratios of chromosome 2 and 18 in two WT replicates and lamin B1-
823 KO replicates. Interaction numbers of chromosome 2 and 18 are normalized by the total
824 interactions of the whole genome in each sample. Mean \pm standard error (SE). * $p < 0.05$, t-
825 test.



826

827 **Fig. 2 Lamin B1 depletion reduces the isolation of chromosome territories and A/B**
828 **compartments**

829 (A) Normalized Hi-C trans-interaction matrices for the whole chromosomes in WT and
830 lamin B1-KO samples.

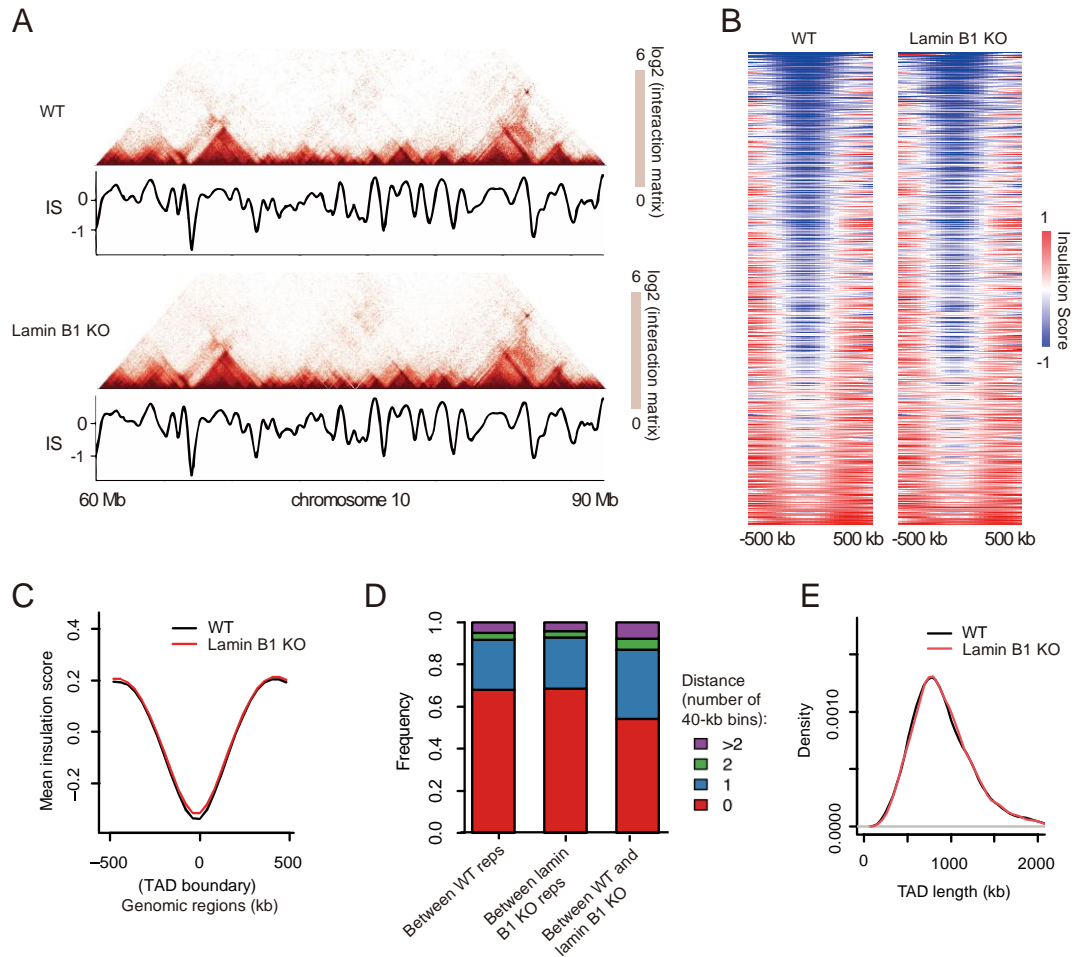
831 (B) Trans-interaction ratios of each chromosome in WT and lamin B1-KO cells. For each
832 chromosome, trans-interaction ratio is the percentage of trans-interaction in total
833 interaction of this chromosome. *** $p < 0.001$, paired t-test. 2 biological repeats.

834 (C) Normalized Hi-C interaction matrices for chromosome 2 (110-190 Mb) in WT and
835 lamin B1-KO cells, and differential matrices of genomic regions between WT and lamin
836 B1-KO cells (resolution: 200 kb). Below the heatmaps are PC1 values and gene density
837 plots. Orange represents compartment A, and blue represents compartment B. High gene
838 density regions correlate with compartment A.

839 (D) Ratios of inter-compartment interactions (AB) and intra-compartment interactions
840 (AA+BB) for each chromosome (X chromosome excluded) in WT and lamin B1-KO
841 cells. * $p < 0.05$, paired t-test. 2 biological repeats.

842 (E) Example of genomic region transition from A compartment in WT cells to B
843 compartment in lamin B1-KO cells. Compartment A (orange, positive PC1 signal) and
844 compartment B (blue, negative PC1 signal) distribution on chromosome 3 (51.5-100 Mb)
845 in WT and lamin B1-KO cells.

846 (F) Genome-wide summary of genomic regions switching between A/B compartments in
847 WT and lamin B1-KO cells. 2 biological repeats.



848

849 **Fig. 3 Lamin B1 is not required for TAD insulation.**

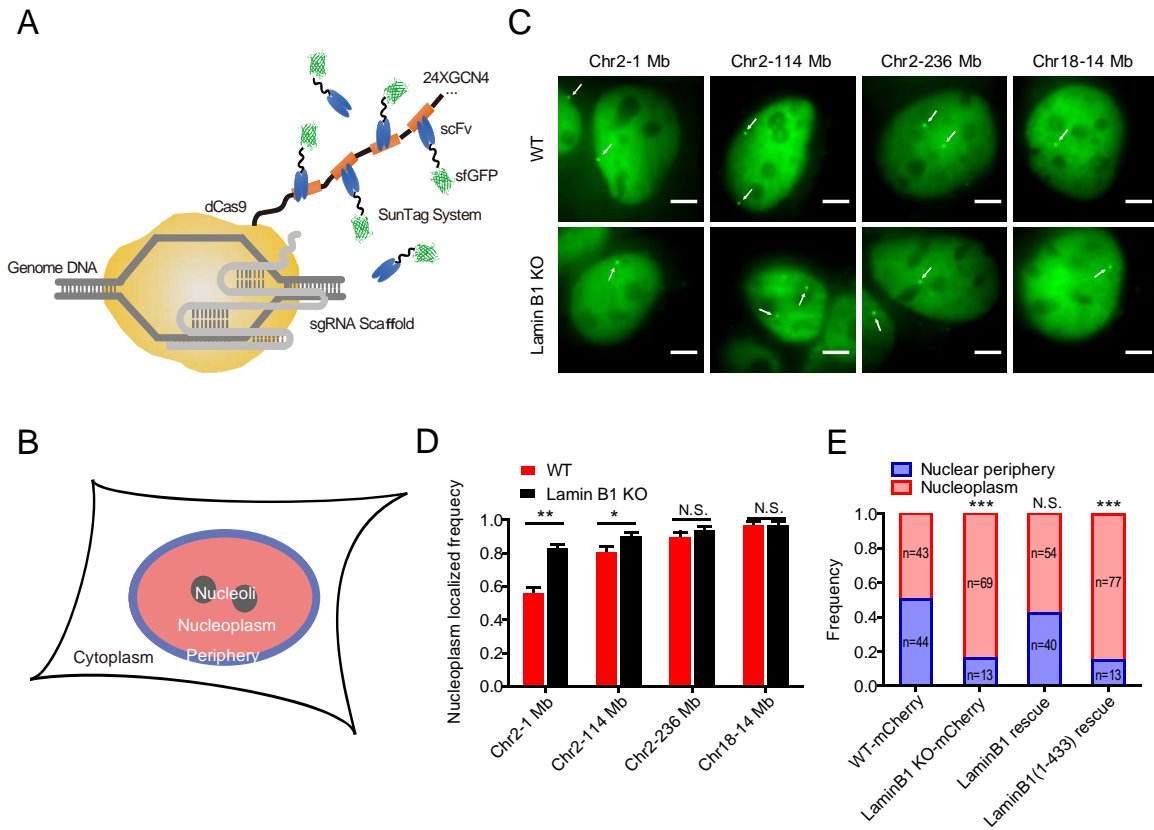
850 (A) Example of TAD pattern and insulation score distribution for chromosome 10 (60-90
851 Mb) in WT and lamin B1-KO cells.

852 (B) Heatmaps of insulation score around TAD boundaries in WT and lamin B1-KO cells.
853 Heatmaps are organized according to the sum of insulation score around each boundary
854 (± 500 kb).

855 (C) Average insulation score distribution around TAD boundaries (± 500 kb) in WT and
856 lamin B1-KO cells. 2 biological repeats.

857 (D) Histogram of distance frequency of the most adjacent TAD boundary pairs between
 858 WT and lamin B1-KO cells, as well as between replicates of WT and lamin B1-KO-cells
 859 (40 kb bin).

860 (E) Distribution of TAD length in WT and lamin B1-KO cells. 2 biological repeats.



861

862 **Fig. 4 Lamin B1 depletion changes the location preference of genomic loci.**

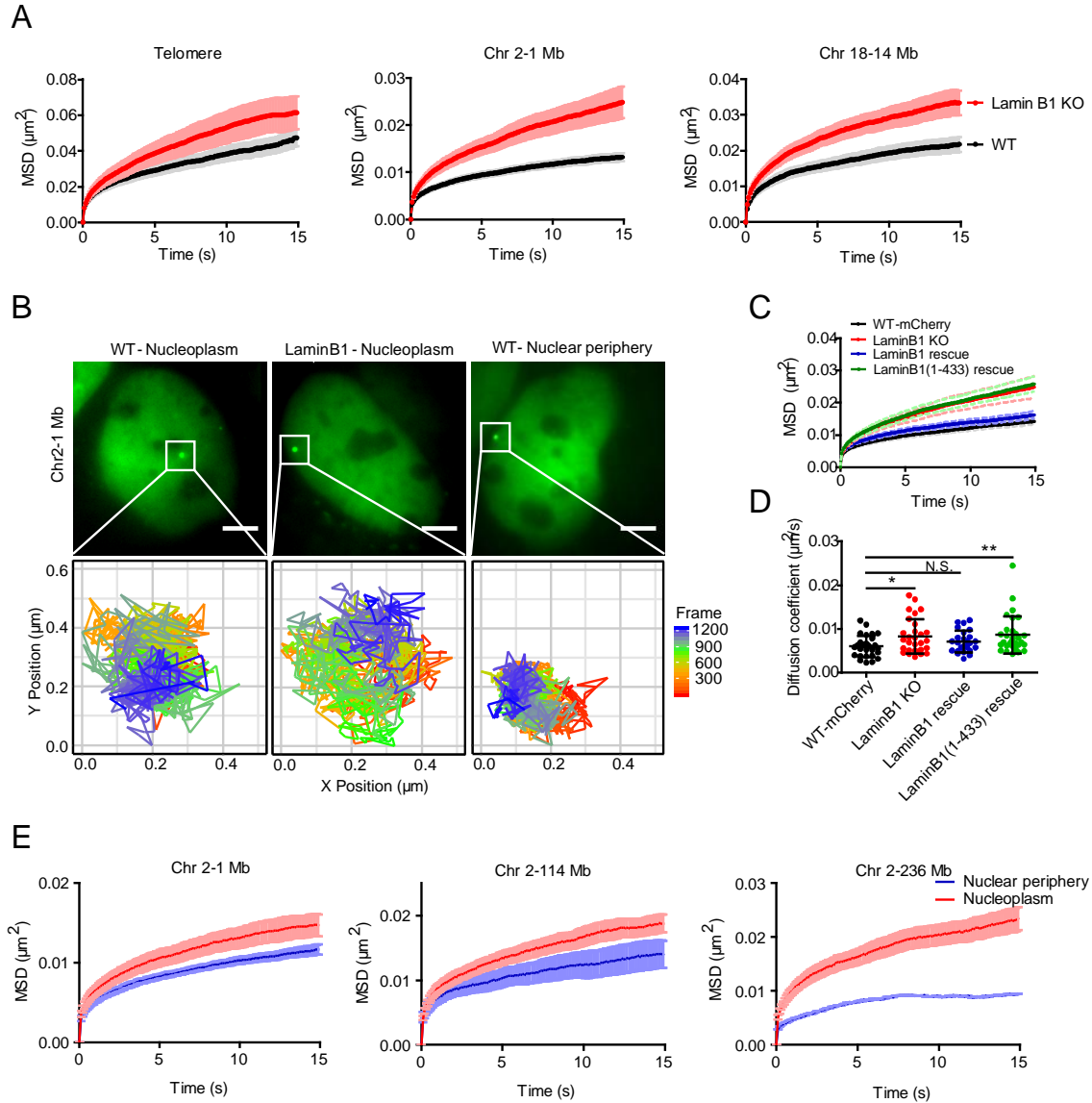
863 (A) Schematic representation of CRISPR-SunTag, a labeling and signal amplification
 864 system including dCas9 fused with 24 tandem repeats of GCN4 peptide and a sfGFP-
 865 tagged single chain antibody (scFv) for GCN4 peptides. Using dCas9-(GCN4)_{24x}
 866 coexpressing with scFv-GCN4-sfGFP at minimal level, a single sgRNA can recruit as
 867 many as 24 fluorescent proteins to the target site.

868 **(B)** Each nucleus is divided into two compartments, nuclear periphery (blue) and
869 nucleoplasm (pink, including nucleoli).

870 **(C)** CRISPR-SunTag labeling of chr2-1 Mb, chr2-114 Mb, chr2-238 Mb and chr18-14 Mb
871 in WT and lamin B1-KO cells. The white arrows show signals of each loci. Scale bars, 5
872 μm .

873 **(D)** The nucleoplasm-localizing frequency of chr2-1 Mb (n=84), chr2-114 Mb (n=117),
874 chr2-238 Mb (n=97) and chr18-14 Mb (n=80) in WT cells, as well as those of chr2-1 Mb
875 (n=88), chr2-114 Mb (n=97), chr2-238 Mb (n=108) and chr18-14 Mb (n=85) in lamin B1-
876 KO cells. ** $p < 0.01$, * $p < 0.05$, unpaired t test. 3 independent experiments.

877 **(E)** The subnuclear localization changes of 1Mb loci in chromosome 2 in mCherry
878 expressing-WT cells (n=87), mCherry expressing-lamin B1-depleted cells (n=82), lamin
879 B1-rescue cells (n=94) and lamin B1(1-433)-rescue cells (n=90). *** $p < 0.001$, Fisher's
880 exact test. 3 independent experiments.



881

882 **Fig. 5 Loss of chromatin-lamin B1 interaction increases chromatin mobility.**

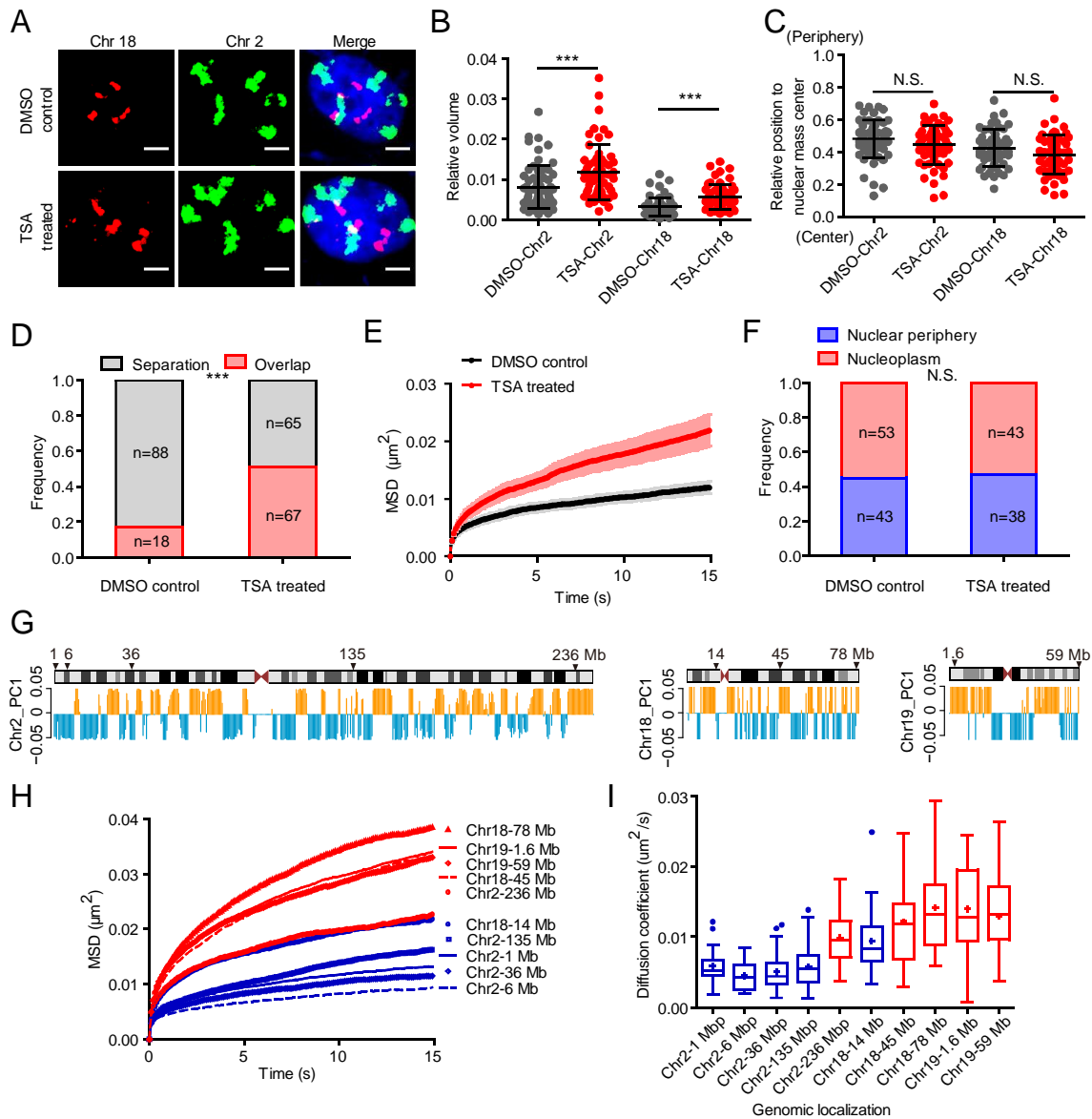
883 (A) MSD curve of telomeres in WT (n=100) and lamin B1-KO (n=86) cells. MSD curves
 884 of 1Mb loci on chromosome 2 in WT (n=27) and lamin B1-KO (n=29) cells. MSD curves
 885 of 14 Mb loci on chromosome 18 in WT (n=28) and lamin B1-KO (n=33) cells. Mean \pm
 886 SE. 3 independent experiments.

887 **(B)** The tracking trajectories of labeled 1Mb loci on chromosome 2 in nucleoplasm of WT
888 cells, nucleoplasm of lamin B1-KO cells and nuclear periphery of WT cells. Different
889 colors of trajectories represent time lapse. Scale bars, 5 μm .

890 **(C)** MSD curve of 1Mb loci in WT (expressing mCherry, n=29), lamin B1-KO (n=29),
891 lamin B1-rescue (n=25) and lamin B1(1-433)-rescue (n=30) cells. Mean \pm SE. 3
892 independent experiments.

893 **(D)** The diffusion coefficient of 1Mb loci in WT (expressing mCherry, n=29), lamin B1-
894 KO (n=29), lamin B1-rescue (n=25) and lamin B1(1-433)-rescue (n=30) cells. Mean \pm SD.
895 * $p < 0.05$, ** $p < 0.01$, unpaired t test. 3 independent experiments.

896 **(E)** 3 genomic loci on chromosome 2 are tracked and assigned to nuclear periphery or
897 nucleoplasm compartment, including 1 Mb loci (n=27), 114 Mb loci (n=30) and 236 Mb
898 loci (n=18). Averaged MSD curves of these loci in the two compartments are calculated
899 and displayed as mean \pm SE. 3 independent experiments.



900

901 **Fig. 6 Global decompaction of chromatin contributes to chromatin dynamics**

902 **increase and chromosome territories intermingling.**

903 (A) Representative 3D-projection chromosome painting images of chromosome 2 and 18

904 in DMSO-treated control cells and TSA-treated cells. Green: FISH signal of chromosome

905 2. Red: FISH signal of chromosome 18. Blue: DAPI staining. The maximum intensity

906 projections of nuclear Z stacks are displayed. Scale bars, 5 μm .

907 **(B)** Quantification of the volumes occupied by chromosome 2 and 18 relative to the nuclear
908 volume. Mean \pm SD. *** $p < 0.001$, Mann–Whitney test. 3 independent experiments.

909 **(C)** Quantification of the nuclear localization of chromosomes based on their relative
910 distances from the chromosome mass center to the nuclear mass center. This distance is
911 normalized by the cubic root of the nuclear volume. Mann–Whitney test. 3 independent
912 experiments.

913 **(D)** Quantification of the overlap frequency between chromosome 2 and chromosome 18
914 territories. The ratio of cells presenting territory interaction between chromosome 2 and
915 chromosome 18 in control cells (n=106) is significantly smaller than TSA-treated cells
916 (n=132). *** $p < 0.001$, Fisher’s exact test. 3 independent experiments.

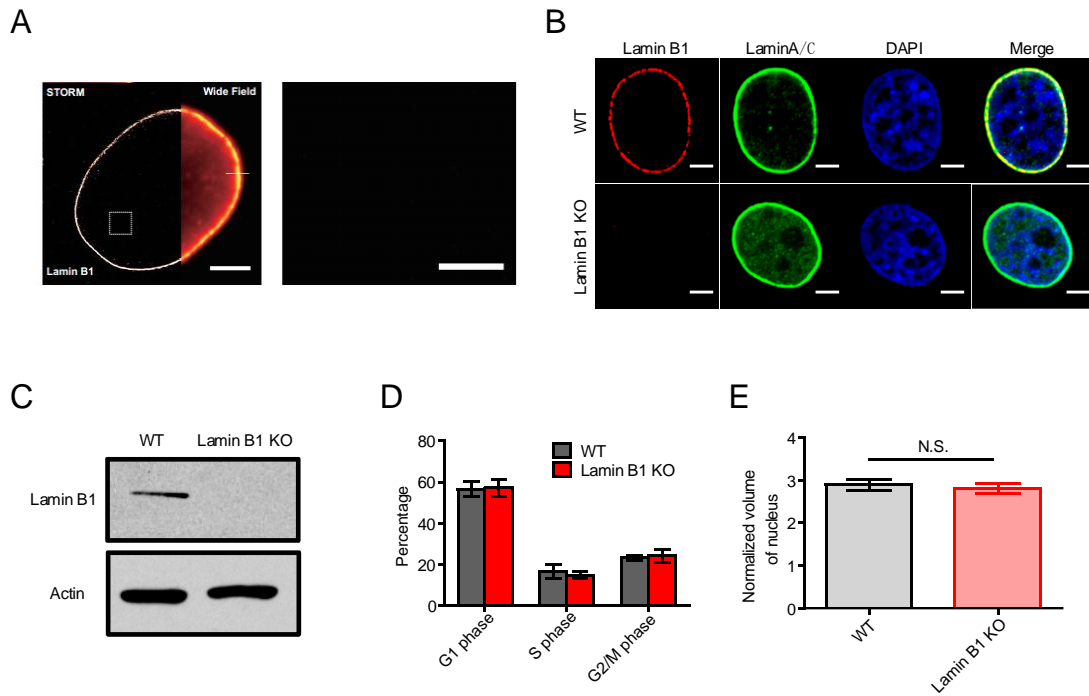
917 **(E)** MSD curves of 1Mb loci on chromosome 2 in DMSO-treated control cells (n=25) and
918 TSA-treated cells (n=26). Mean \pm SE. 3 independent experiments.

919 **(F)** The spatial localization of 1 Mb loci on chromosome 2 in DMSO-treated control cells
920 (n=96) and TSA-treated cells (n=81). Fisher’s exact test. 3 independent experiments.

921 **(G)** Schematic representation and PC1 values plots of chromosome 2, chromosome 18 and
922 chromosome 19. Orange represents compartment A, and blue represents compartment B.
923 Arrows indicate the genomic distribution of chosen loci.

924 **(H)** The averaged MSD curves and **(I)** The diffusion coefficient distribution of 10 genomic
925 loci on chromosome 2, chromosome 18 and chromosome 19. Red indicates loci belonging
926 to A compartment and blue indicates loci belonging to B compartment. 3 independent
927 experiments.

928 Supplementary Figures



929

930 Fig. S1 Preparation of lamin B1 knock-out (KO) cell lines.

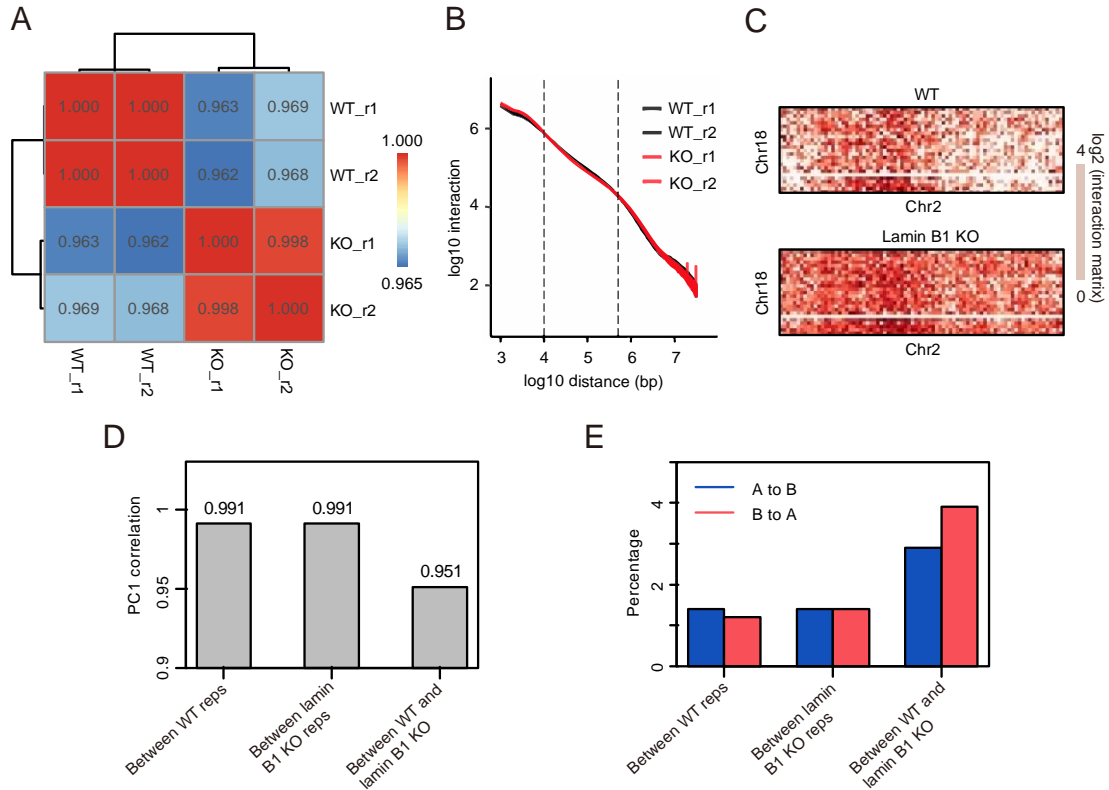
931 (A) STORM image and wide-field image of lamin B1 in MDA-MB-231 cells. Scale bar:
932 5 μ m. Magnified image of the boxed area shows that lamin B1 almost has no presence in
933 nucleoplasm. Scale bar: 1 μ m.

934 (B) Immunofluorescence of chosen lamin B1-KO clone with lamin B1 and lamin A/C
935 antibody. WT MDA-MB-231 cell line is used as positive control. The result indicates that
936 lamin B1 is totally knocked out in the chosen KO clone, while lamin A/C is unaffected.
937 The images are shown under the same intensity threshold between WT and lamin B1-KO
938 cells.

939 (C) Western blot of chosen lamin B1 KO clone with lamin B1 antibody. Actin is used as
940 loading control. WT MDA-MB-231 cell line functions as positive control.

941 (D) Percentage of cells in G1, S, and G2/M phase in 3 independent experiments.

942 (E) Quantification of nuclear volume based on DAPI staining in WT (n=18) and lamin
943 B1-KO (n=16) cells. Mean \pm SE. Nuclear volumes of the two samples do not have
944 significant difference.



945

946 **Fig. S2 Reproducibility analysis of Hi-C data.**

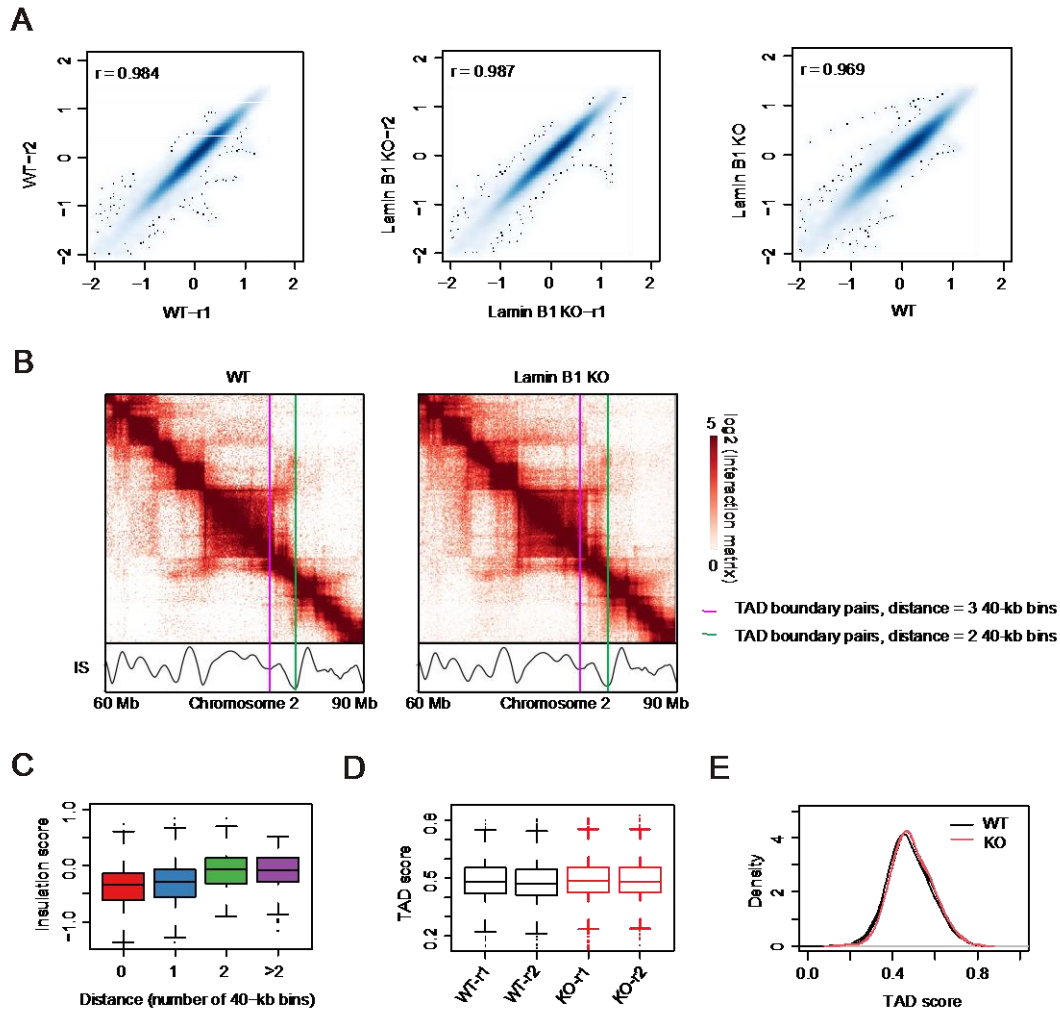
947 (A) Pearson correlation coefficients of the whole genome interaction matrices (resolution:
948 500 kb) of WT and lamin B1-KO replicates.

949 (B) Hi-C interaction frequency as a function of genomic linear distance for WT and lamin
950 B1-KO replicates.

951 (C) Normalized Hi-C trans-interaction matrices for chromosome 2 and 18 in WT and
952 lamin B1-KO samples.

953 (D) Pearson correlation coefficients of the whole genome PC1 values between WT
954 replicates ($r=0.991$), lamin B1-KO replicates ($r=0.991$), WT and lamin B1-KO samples
955 ($r=0.951$).

956 (E) Percentage of the whole genome A/B compartment transition between WT replicates,
957 lamin B1-KO replicates, WT and lamin B1-KO samples.



958

959 **Fig. S3 TAD analysis.**

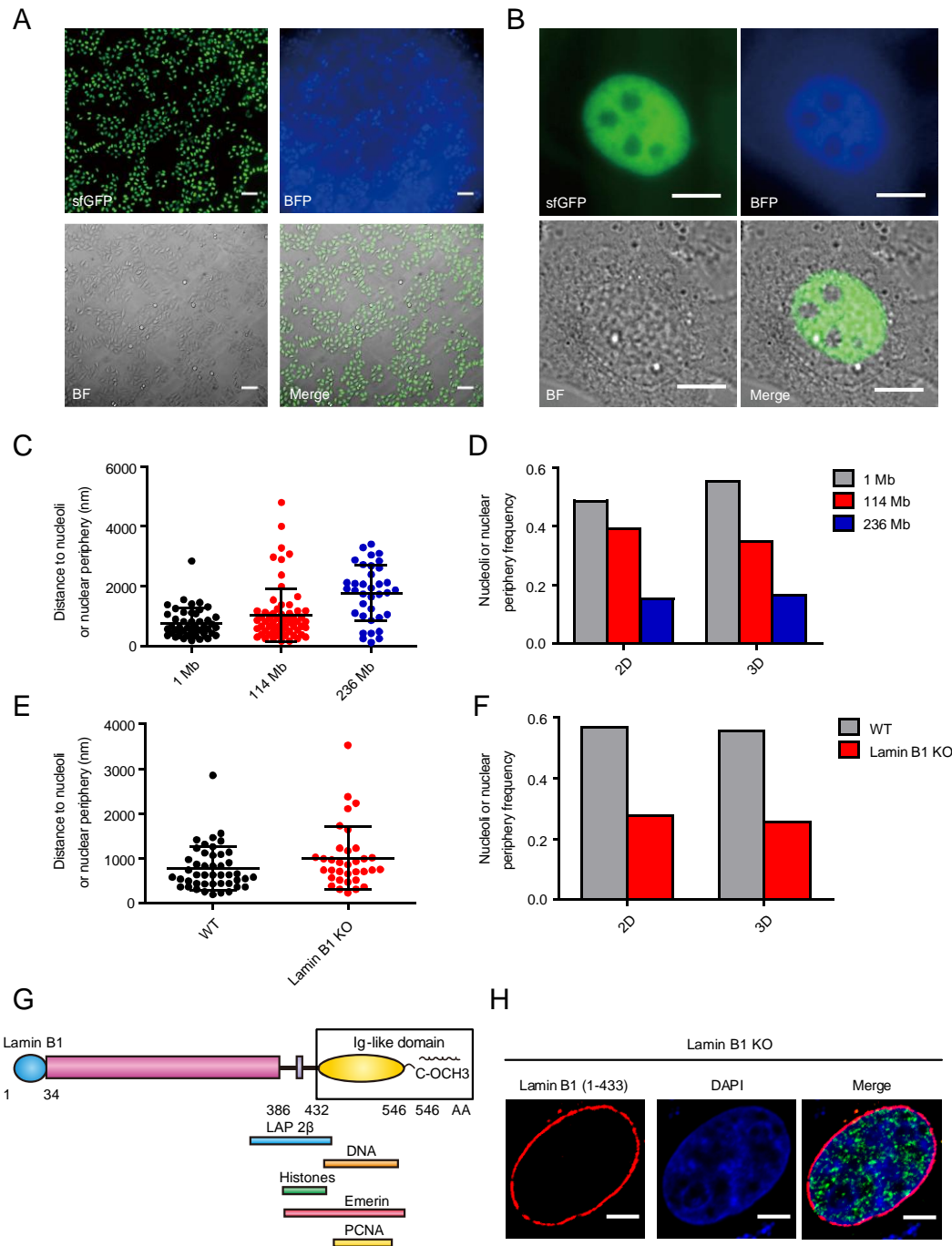
960 (A) Scatter plots of the whole genome insulation scores of WT replicates (left, Pearson
961 correlation coefficient $r=0.984$), lamin B1-KO replicates (middle, Pearson correlation
962 coefficient $r=0.987$), WT and lamin B1-KO samples (right, Pearson correlation
963 coefficient $r=0.969$).

964 (B) Example of two most adjacent TAD boundary pairs in WT and lamin B1 KO-cells,
965 with the distance of 3 (purple) and 2 (green) 40-kb bins.

966 (C) Boxplot of mean insulation scores of most adjacent TAD boundary pairs in WT and
967 lamin B1-KO cells at a distance of indicated numbers. Together with Fig. S3B, the
968 insulation score valleys at identical boundary pairs are lower and sharper than the
969 changed ones, indicating that shifted TAD boundaries are due to variance upon
970 calculation.

971 (D) Boxplot of TAD scores of WT and lamin B1-KO replicates. TAD score=intra-TAD
972 interactions / (intra- + inter-TAD interactions).

973 (E) TAD score distribution of WT and lamin B1-KO samples.

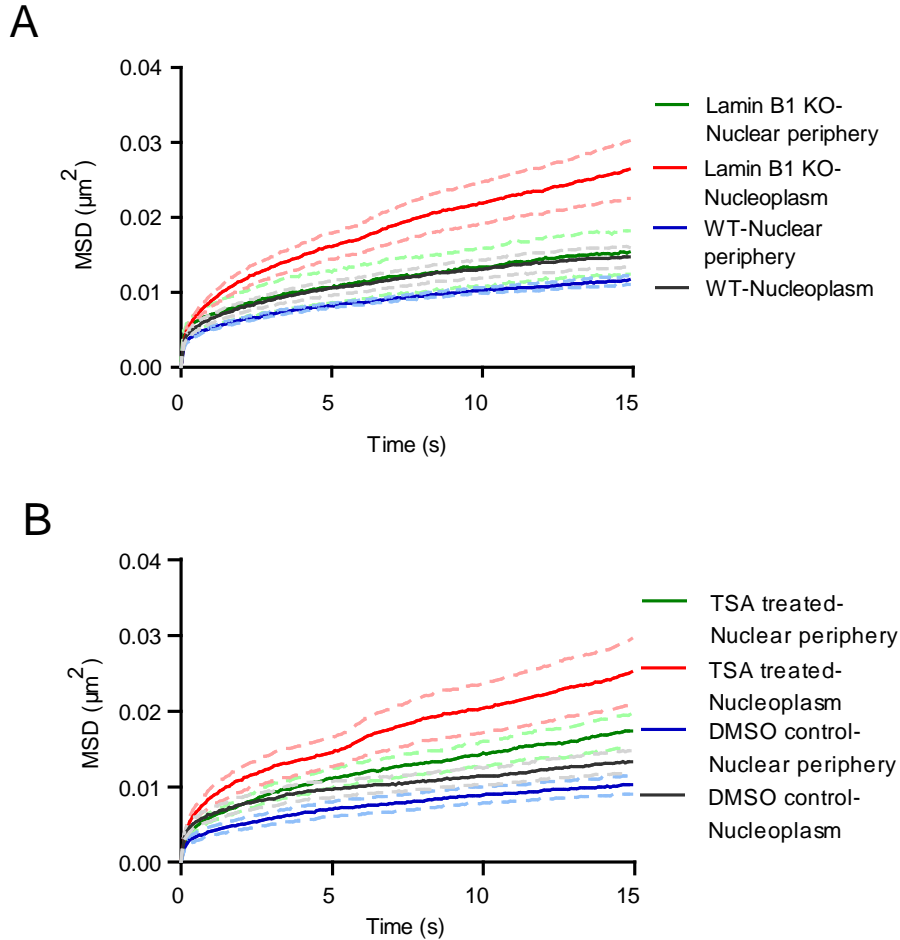


974

975 **Fig. S4 Construction of SunTag stable cell line, comparison between 2D and 3D**
 976 **images and description of lamin B1 truncation.**

977 (A) Fluorescent images of the SunTag cell line under 10X magnification with Dox
 978 induction. BFP and bright field (BF) are also shown. All cells display similar expression
 979 level of both dCas9-(GCN4) X24 and scFv-GCN4-sfGFP. Scale bars: 100 μ m.

- 980 **(B)** Fluorescent images of the SunTag cell line under 100X magnification with Dox
981 induction. BFP and bright field (BF) are also shown. The absence of fluorescent signal of
982 both blue and green channel in nucleoli indicates that this method is superior to the
983 conventional dCas9-GFP labeling method which shows severe nucleoli aggregation.
984 Scale bars: 10 μ m.
- 985 **(C)** Quantification of distance from three genomic loci on chromosome 2 to nucleolus or
986 nuclear periphery in reconstructed 3D images. 2 independent experiments.
- 987 **(D)** Nucleoli and nuclear periphery localization frequency of 3 genomic loci on
988 chromosome 2 from 2D and 3D images. Each locus is assigned to this localization
989 according to the rule that the minimum distance to nucleoli or nuclear envelope is less
990 than 4 pixels (\sim 640 nm).
- 991 **(E)** Quantification of distance from 1 Mb locus on chromosome 2 to nucleolus or nuclear
992 periphery in WT and lamin B1-KO cells in reconstructed 3D images. 2 biological repeats.
- 993 **(F)** Nucleoli and nuclear periphery localization frequency of 1 Mb locus on chromosome
994 2 from 2D and 3D images. Each locus is assigned to this localization according to the
995 rule that the minimum distance to nucleoli or nuclear envelope is less than 4 pixels (\sim 640
996 nm).
- 997 **(G)** Diagram of lamin B1 and binding sites of interaction partners. The Ig-like domain of
998 lamin B1 mediates direct and indirect interaction between lamin B1 and chromatin
999 through DNA and other proteins.
- 1000 **(H)** Lamin B1 (1-433) truncation without Ig-like domain localizes in nuclear periphery
1001 when expressed in lamin B1-KO cells.

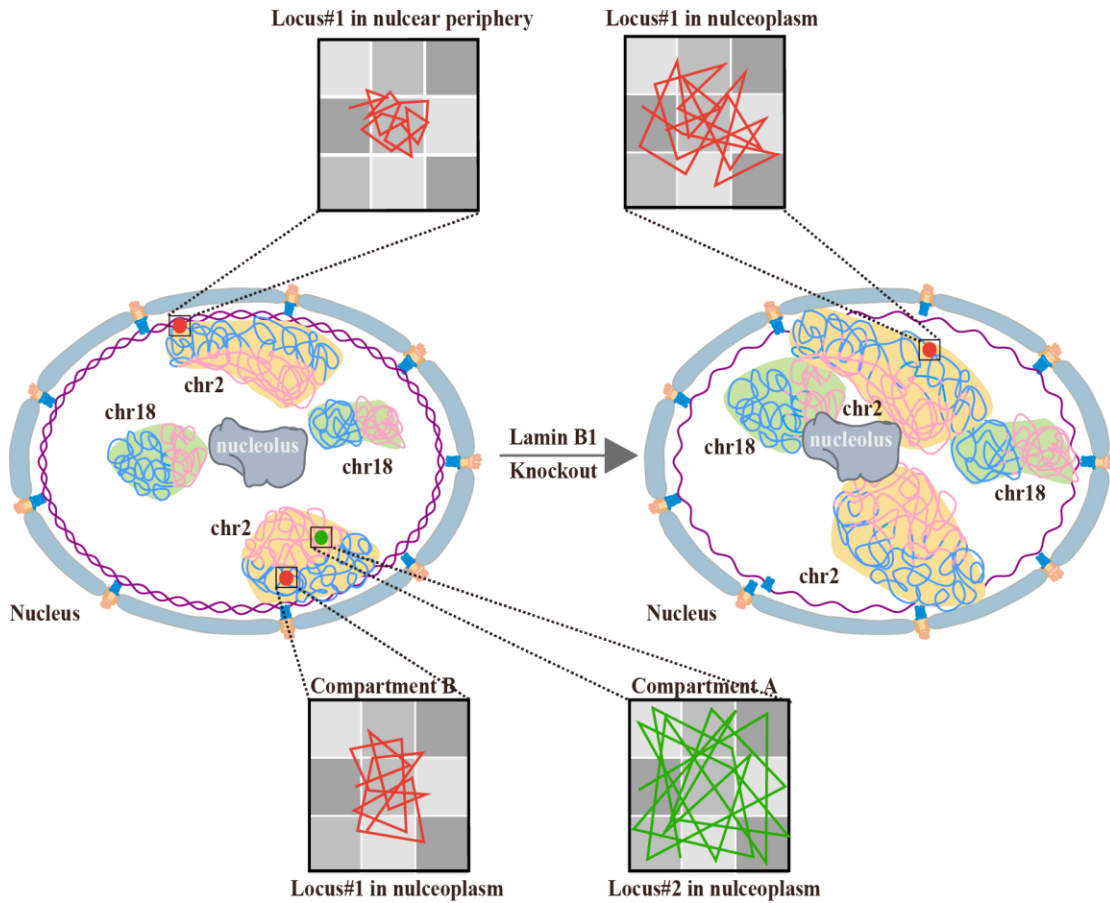


1002

1003 **Fig. S5 MSD curves of 1Mb loci on chromosome 2.**

1004 (A) MSD curves of 1Mb loci on chromosome 2 localized in nuclear periphery and
1005 nucleoplasm of WT and lamin B1-KO cells, separately. Mean \pm SEM. Depletion of lamin
1006 B1 increases 1Mb loci dynamics in both periphery and nucleoplasm. 3 independent
1007 experiments.

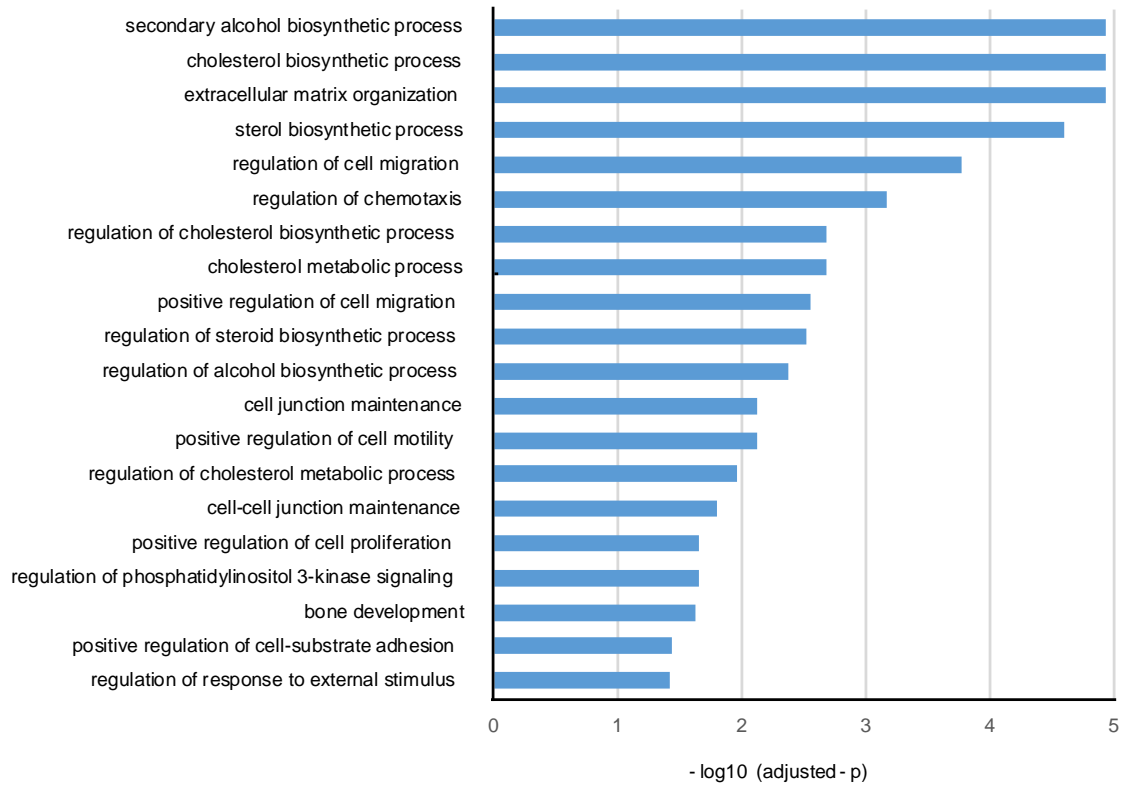
1008 (B) MSD curves of 1Mb loci on chromosome 2 localized in nuclear periphery and
1009 nucleoplasm of DMSO-treated control and TSA-treated cells, separately. Mean \pm SEM.
1010 TSA treatment increases 1Mb loci dynamics in both nuclear periphery and nucleoplasm.
1011 3 independent experiments.



1012

1013 Fig. S6 Model.

1014 A model describing lamin B1 regulating chromatin higher-order structure and dynamics
1015 through tethering to chromatin. Loss of lamin B1 in lamina releases a part of chromatin
1016 from nuclear periphery to nuclear interior. The change of chromosome compaction state
1017 induces expansion of chromosome territories and thus increases the interaction ratio
1018 between different chromosomes. Besides, loss of lamin B1 reduces the integrity and
1019 segregation of chromatin compartments and part of genomic regions switches between A
1020 and B compartments. However, lamin B1 is not required for TAD insulation.
1021 Furthermore, depletion of lamin B1 can increase genomic loci dynamics. The dynamic
1022 motion of the same locus in different subnuclear regions demonstrates significant
1023 difference, and nuclear periphery-localized loci is much less mobile than the
1024 nucleoplasmic-positioned loci. Besides, chromatin compaction is a more fundamental
1025 factor affecting chromatin dynamics. Genomic loci in less compact compartment A are of
1026 higher mobility than those in more compact compartment B.



1027

1028 **Fig. S7 GO (Biological Process) analysis of down-regulated genes upon lamin B1**
1029 **KO.**

1030

1031 **Table S1 Quality control statistics for Hi-C data processing.**

| | WT-r1 | WT-r2 | Lamin B1 KO-r1 | Lamin B1 KO-r2 |
|--|-----------------------|-----------------------|-----------------------|-----------------------|
| Total read pairs^[1] | 138,193,618 | 223,885,207 | 250,362,318 | 253,024,668 |
| Uniquely aligned read pairs^[2] | 108,155,179 78.26% | 172,561,205 77.08% | 182,642,642 72.95% | 194,536,722 76.88% |
| Valid interaction^[3] | 95,264,155 88.08% | 152,469,233 88.36% | 148,123,567 81.10% | 166,884,723 85.79% |
| Self-Circle^[4] | 123,564 0.11% | 178,371 0.10% | 520,046 0.28% | 222,818 0.11% |
| Dangling-end^[5] | 2,726,851 2.52% | 4,213,273 2.44% | 13,818,685 7.57% | 6,521,973 3.35% |
| Valid interaction rmdup^[6] | 79,041,927 73.08% | 131,026,015 75.93% | 129,693,005 71.01% | 134,947,244 69.37% |
| Trans_interaction^[7] | 7,834,781 9.91% | 13,603,317 10.38% | 15,747,086 12.14% | 16,307,003 12.08% |
| Cis_interaction^[8] | 71,207,146 90.09% | 117,422,698 89.62% | 113,945,919 87.86% | 118,640,241 87.92% |
| Cis_shortRange^[9] | 22,113,855 31.06% | 34,770,742 29.61% | 37,869,246 33.23% | 39,050,597 32.92% |
| Cis_longRange^[10] | 49,093,291 68.94% | 82,651,956 70.39% | 76,076,673 66.77% | 79,589,644 67.08% |

1032 The percentage denominators of [2] are the read pair numbers in [1]; the percentage
 1033 denominators of [3][4][5][6] are the uniquely aligned read pair numbers in [2]; the
 1034 percentage denominators of [7][8] are in [6]; and the percentage denominators of [9][10]
 1035 are in [8].